Correspondence to:
M. Andrés-Martínez,
andresma@uni-bremen.de

Thermomechanical Implications of Sediment Transport for the Architecture and Evolution of Continental Rifts and Margins

Miguel Andrés-Martínez[1] , **Marta Pérez-Gussinyé[1]** , **John Armitage[2]** , and **Jason P. Morgan[3]**

[1]MARUM-Center for Marine Enviromental Sciences, University of Bremen, Bremen, Germany, [2]Institut de Physique du Globe de Paris, France, [3]Royal Holloway, University of London, London, UK

Abstract Erosion and deposition redistribute mass as a continental rift evolves, which modifies crustal loads and influences subsequent deformation. Surface processes therefore impact both the architecture and the evolution of passive margins. Here we use coupled numerical models to explore the interactions between the surface, crust, and lithosphere. This interaction is primarily sensitive to the efficiency of the surface processes in transporting mass from source to sink. If transport is efficient, there are two possible outcomes: (1) Faulting within the zone of extension is longer lived and has larger offsets. This implies a reduction of the number of faults and the width of the proximal domain. (2) Efficient transport of sediment leads to significant deposition and hence thermal blanketing. This will induce a switch from brittle to ductile deformation of the upper crust in the distal domains. The feedbacks between these two outcomes depend on the extension history, the underlying lithospheric rheology, and the influence of submarine deposition on sediment transport. High erosion/sedimentation during early faulting leads to abrupt crustal necking, while intermediate syntectonic sedimentation rates over distal deep submarine hotter crust leads to unstructured wide distal domains. In models where rheological conditions favor the formation of asymmetric conjugate margins, only subaerial transport of sediments into the distal domains can increase conjugate symmetry by plastic localization. These models suggest that passive margin architecture can be strongly shaped by the solid Earth structure, sea level, and climatic conditions during breakup.

1. Introduction

Rifting is a fundamental stage in the Wilson cycle. Although easy to idealize in plate tectonics, rifting is quite complex as multiple processes and their feedbacks appear to play a significant role. These processes range from erosion and sedimentation at the surface to deeper processes such as faulting, flexure due to loading/unloading, lithospheric and crustal thinning, mineral phase changes, convection, mantle exhumation, melting, and melt emplacement. Numerous studies have shown how the broad variety of passive margin architectures around the world can potentially be explained by variations in extension velocity, initial thermal state, rheology, and precursor structures within the lithosphere in which these margins formed (e.g., Brune et al., 2014; Buck, 1991; Huismans & Beaumont, 2003, 2007, 2014; Ros et al., 2017; Sharples et al., 2015; Svartman Dias et al., 2015).

Some recent studies, however, have started to point out the influence of surface processes (SP; i.e., erosion and sedimentation) in shaping rift architecture. For example, in the Gulf of California, more magmatically robust and narrow margins develop in the northern sector (Delfín-Tiburón and Guaymas sector), while less magma rich and wide margins develop in the south central sector (Alarcon sector). Lizarralde et al. (2007) suggested that these differences occur at a length-scale too small to be explained by the above mentioned factors and argued that the variation in architecture along the margin is due to different degrees of mantle fertility/hydration between the north (fertile) and the south (less fertile) aided by higher sediment deposition in the north that leads to an increase in melting due to thermal blanketing.

Surface processes have also been invoked to explain the post-rift evolution of margins, such as the observed persistence of rift shoulder uplift after breakup, through trade-offs between flexural bending, unloading at the shoulder due to erosion, and loading at the marginal basins due to sedimentation (Burov & Cloetingh, 1997; Petit et al., 2007; Redfield & Osmundsen, 2013; Weissel & Karner, 1989). Additionally, Morley and

Westaway (2006) and Clift et al. (2015) showed that during the post-rift period, an increase of sediment influx into marine basins related to a change in climate is capable of inducing ductile lower crustal flow and larger subsidence rates than expected from thermal subsidence. Furthermore, Petit et al. (2007) showed that climate can also influence post-rift escarpment morphology.

Numerical studies have analyzed how surface processes can have an effect on both shallow and deeper Earth dynamics. In passive margins, surface mass transport changes the crustal strength and flexural stresses, and can trigger lower crustal flows that enhance subsidence and rifting (Burov & Cloetingh, 1997; Burov & Poliakov, 2001). During rifting an input of sediments from far-field sources have proven to favor narrow rifting because the loads reduce the buoyancy force difference between the shoulders and the center of the rift, which avoids rift migration (Bialas & Buck, 2009), and also to control the mode transition from asymmetric basins to symmetric due to loading of the hanging wall (Buiter et al., 2008). Olive et al. (2014) showed that active surface processes increase the life span of faults and the amount of horizontal strain that they can accommodate. This occurs because surface processes reduce the topographic and flexural force working against the active fault (Olive et al., 2014). Through analog modeling, Zwaan et al. (2018) showed that sedimentation at grabens and half-grabens aids localization of deformation, enhances fault offsets, reduces hanging wall structure, attenuates lower crustal exhumation, and sustains high angles at faults for a longer period of time, although 3-D rift structure is not significantly affected.

Previous studies focused on particular aspects of SP-tectonic feedbacks such as the effect of SP in the mechanics of a single fault (Olive et al., 2014), the ability of SP to trigger narrow rifting mode through sedimentation (Bialas & Buck, 2009), how SP shape the number of simultaneous active faults and faulting symmetry (Buiter et al., 2008), or how the timing of salt deposition during rifting affects the final salt distribution (Allen & Beaumont, 2016). These works, with the exception of Allen and Beaumont (2016), use relatively simple setups that lack nonlinear and/or temperature-dependent viscosities in the lower crust or lack elasticity and/or a realistic landscape evolution model (e.g., lack of erosion and filling the basin up to a base level). In this work we develop and use a finite element numerical model which fully couples subaerial and submarine landscape evolution to lithospheric extension. We do this by solving sediment transport, mass, momentum, and energy conservation equations. Our focus is to analyze in detail the effects that thermal insulation and stress loading due to sedimentation have on the deformation mode during extension and on the final margin architecture. Finally, we analyze how the occurrence of slower deep submarine SP during the late stages of rifting may modulate the rift geometry. For this purpose we conduct a parametric study in which we vary crustal thickness, lower crustal rheology, the efficiency of subaerial SP, and the presence/absence of sea and hence submarine erosion and sediment transport. This approach allows us to investigate three main unresolved questions regarding the interplays between surface processes and tectonics: (1) how loading/unloading through surface processes interacts with thermal blanketing to shape passive margins; (2) where in space and time loading/unloading versus thermal blanketing effects are dominant, and how these effects are modulated by the initial strength of the crust; and (3) what role the timing of marine incursion plays in the distribution of sediments and final margin architecture. Finally, we use these results to discuss structural differences between natural examples of margins that display different amounts of syn-rift sedimentation.

2. Methodology

In order to address the previously discussed questions, we have developed a new 2-D visco-elasto-plastic geodynamic model based on MILAMIN mechanical and thermal solvers (Dabrowski et al., 2008). The code simulates dynamic topography by using a stress-free surface (Andrés-Martínez et al., 2015; Kaus et al., 2010) and accounts for strain softening, shear heating, and surface processes calculated from a sediment transport model. Below we first describe the tectonic model, then the geomorphologic model, and finally how they are coupled.

2.1. Tectonic Model

We model a 2-D section of the continental lithosphere and upper asthenosphere which is divided in three layers with different thermomechanical properties: (1) upper crust (UC), (2) lower crust (LC), and (3) mantle. Mantle includes an upper section (i.e., lithospheric mantle) consisting of dryer olivine and a deeper asthenospheric section, consisting of wetter olivine, separated by a 5-km transition zone. Mantle rheologies

are calculated based on depletion values and tracked with the material flow along time. The model domain is subjected to half-extension velocities on the sides to simulate far-field stretching.

Our model calculates deformation and pressure by solving (1) the Stokes force-balance equation for incompressible viscous flow (equation (1)) and (2) the equation for mass conservation (equation (2)):

$$\nabla \cdot \tau - \nabla P + \rho g = 0, \tag{1}$$

$$\nabla \cdot v = 0, \tag{2}$$

where τ is the deviatoric stress, P is the total pressure, ρ is the density, g is the gravitational acceleration, and v is the velocity (e.g., Dabrowski et al., 2008; Kaus, 2010; Moresi et al., 2003).

Temperatures are solved using the heat conservation equation:

$$\rho C_p \frac{DT}{Dt} = \nabla \cdot (k \nabla T) + H_r + H_s, \tag{3}$$

where C_p is the heat capacity, T is temperature, t is time, k is thermal conductivity, and H_r and H_s are the radioactive and shear heating volumetric heat productions, respectively.

The constitutive relation between shear stress τ and strain rate $\dot{\varepsilon}$ is

$$\tau = \eta_{eff} \left(2\dot{\varepsilon}' + \frac{\tau^{old_J}}{\mu \Delta t} \right), \tag{4}$$

where η_{eff} is the effective or numerical viscosity, $\dot{\varepsilon}'$ is the deviatoric strain rate, τ^{old_J} accounts for previous time step rotated stresses resulting from applying finite-difference time discretization to the Jaumann objective derivative to include elastic behavior (Kaus, 2010; Moresi et al., 2003), μ is the shear modulus, and Δt is the time step.

To calculate the effective viscosity η_{eff} we first need to evaluate whether the material behaves plastically or viscoelastically. For that purpose we adopt the Drucker-Prager yield criterion which implies that yielding is met when the square root of the second invariant of the deviatoric stress (τ_{II}) is larger than the yield stress σ_{yield}, defined as

$$\sigma_{yield} = P sin\phi + C cos\phi, \tag{5}$$

where ϕ and C are the friction angle and the cohesion of the rocks, respectively (e.g., de Souza Neto et al., 2008). In order to include plasticity into the viscous formulation we use Prandtl-Reuss flow rule, which brings τ_{II} to the yield envelope ($\tau_{II} = \sigma_{yield}$) for yielding materials, defining the effective viscosity η_{eff} as

$$\eta_{eff} = \frac{\sigma_{yield}}{\left(2\dot{\varepsilon} + \frac{\tau^{old_J}}{\mu \Delta t} \right)_{II}}, \tag{6}$$

where $()_{II}$ represents the square root of the second invariant operator (Moresi et al., 2003).

If $\tau_{II} < \sigma_{yield}$ then the material behaves viscoelastically and we define effective viscosity η_{eff} as

$$\eta_{eff} = \left(\frac{1}{\eta_{dis}} + \frac{1}{\eta_{dif}} + \frac{1}{\Delta t \mu} \right)^{-1}, \tag{7}$$

where η_{dis} and η_{dif} are dislocation and diffusion creep viscosities, respectively, such as

$$\eta_{dis/dif} = F B^{-\frac{1}{n}} \dot{\varepsilon}_{II}^{\frac{1-n}{n}} exp \left(\frac{E^* + PV^*}{nRT} \right), \tag{8}$$

where F is a factor to scale parameters obtained from uniaxial/triaxial experiments (defined for principal stresses) to our second-invariant-based formulation of the viscosity, B is the pre-exponential factor of the flow law, n is the power law exponent, $\dot{\varepsilon}_{II}$ is the square root of the second invariant of the strain rate, E^* is the activation energy, V^* is the activation volume, R is the gas constant, and T is the absolute temperature. The values of these parameters for both diffusion and dislocation mechanisms and rocks are shown in Table 1. Here we use a wet quartzite flow law to simulate upper crustal deformation (Gleason & Tullis, 1995). Lower crust is expected to be more mafic than the upper crust and feldspar flow laws are expected to represent its

Table 1
Model Parameters

Thermomechanical parameters	Wet quartzite (UC and weak LC)	Wet anorthite (intermediate strength LC)	Mafic granulite (strong LC)	Dry olivine (lithospheric mantle)	Wet olivine (asthenospheric mantle)
Dislocation pre-exponential factor $log(B_{dis})$ [Pa^{-n} s^{-1}]	−28.0	−15.40	−21.05	−15.96	−15.81
Dislocation exponent n_{dis}	4.0	3.0	4.2	3.5	3.5
Dislocation activation energy E^*_{dis} [kJ mol^{-1}]	223	356	445	530	480
Dislocation activation volume V^*_{dis} [10^{-6} m^3 mol^{-1}]	0	0	0	13	10
Diffusion pre-exponential factor $log(B_{dif})$ [Pa^{-1} s^{-1}]	-	-	-	−8.16	−8.64
Diffusion exponent n_{dif}	-	-	-	1	1
Diffusion activation energy E^*_{dif} [kJ mol^{-1}]	-	-	-	375	335
Diffusion activation volume V^*_{dif} [10^{-6} m^3 mol^{-1}]	-	-	-	6	4
	UC	LC	Lithospheric mantle	Asthenospheric mantle	
Shear modulus μ [GPa]	36	40	74	74	
Thermal conductivity k [W m^{-1} K^{-1}]	2.1	2.5	3.3	3.3	
Heat capacity C_p [J kg^{-1} K^{-1}]	1,200	1,200	1,200	1,200	
Radiogenic heat production H_r [μW m^{-3}]	1.3	0.2	0	0	
Reference densities ρ_0 [kg m^{-3}]	2,700	2,850	3,300	3,300	
Thermal expansivity coefficient α_T [10^{-5} K^{-1}]	2.4	2.4	3.0	3.0	

Constants		Value	References
Triaxial scaling parameter		$F = \dfrac{1}{2^{\frac{n-1}{n}}\, 3^{\frac{n+1}{2n}}}$	
Depletion factor for density dependence β		0.041	
Surface processes parameters		**Value**	
Surface processes time step δt_s [Kyr]		1	
Subaerial hillslope diffusion K [m^2 year^{-1}]		0.25	Armitage et al. (2015)
Subaerial discharge transport coefficient c	Low transport	10^{-4}, 5 × 10^{-4}	Paola et al. (1992)
	→	10^{-3}, 5 × 10^{-3}	Marr et al. (2000)
	High transport	10^{-2}, 5 × 10^{-2}	Armitage et al. (2014)
Precipitation rate α [m year^{-1}]		1	Huffman et al. (2009)
Submarine diffusion coefficient K_s [m^2 year^{-1}]		10^2	Kaufman et al. (1991)
Submarine diffusion coefficient decay λ_s [m^{-1}]		5 × 10^{-4}	Kaufman et al. (1991)

Note. Rheological parameters from Wilks and Carter (1990); Gleason and Tullis (1995); and Hirth and Kohlstedt (2003). Depletion factor for density dependency from Schutt and Lesher (2006). Remaining parameters from Turcotte and Schubert (2002). Diffusion creep B is calculated using a grain size d of 6 mm. Wet olivine water content is 500 ppm H/Si. UC = upper crust; LC = lower crust.

rheology (Christensen & Mooney, 1995; Contrucci et al., 2004; Dean et al., 2000; França & Assumpção, 2004; Hopper et al., 2007). We choose to run different models using two end member flow laws for the lower crust: a strong mafic granulite (GR; chosen to amplify brittle tectonic-surface trade-offs), and a weak wet quartzite (WQ; chosen to amplify ductile ones; Gleason & Tullis, 1995; Wilks & Carter, 1990). In order to reproduce an intermediate lower crustal strength, we run models with a third lower crustal flow law: wet anorthite (AN; Rybacki & Dresen, 2000), as it is weaker than the GR from Wilks and Carter (1990), but still representative of mafic materials (see strength profiles in supporting information Figure S2). Lithospheric mantle is simulated as dry olivine, and asthenosphere as wetter olivine (500 ppm H/Si; Brune et al., 2012; Hirth & Kohlstedt, 2003).

After discretization of the spatial domain we use the finite element method to numerically solve equations (1)–(3). Here, we use a triangular grid with resolutions of 1 km in the UC, 5 km in the LC, and 5 km in the mantle, tracked along with the material (Lagrangian mesh). We use Triangle Mesh Generator package (Shewchuk, 2002) in order to produce the finite element grids. Mesh is subdivided in layers of different properties where layer interfaces coincide with element boundaries so that no drastic property changes occur inside the element but along element boundaries. Furthermore, Triangle increases resolution where layers are thinner than the specified resolution, ensuring that deformation is well resolved at thinned layers (e.g., regions of very attenuated lower crust). When large deformations take place in the Lagrangian mesh (i.e., in shear zones), this can result in extremely elongated triangles, in which case the finite element method may not return an accurate solution for the system. In order to avoid this issue, a remesh with a subsequent resampling of the variables is applied. The resampling of variables is done within elements using shape functions for interpolation. This, together with resampling occurring only when necessary (i.e., not in every time step), limits the amount of numerical diffusion of the variables.

We assume rock density ρ is a function of temperature T and, for mantle rocks, also of the degree of depletion (Armitage et al., 2013; Nielsen & Hopper, 2004; Parmentier & Morgan, 1990; Schutt & Lesher, 2006):

$$\rho = \rho_0 \left(1 - \alpha(T - T_0) - \beta D\right), \tag{9}$$

where ρ_0 is the reference density at room temperature T_0, α is thermal expansivity, and β is a factor multiplying the depletion D (Table 1).

Additionally, the model includes a stress-free surface at the top of the model with a free-surface stabilization algorithm (Andrés-Martínez et al., 2015; Kaus et al., 2010) in order to accurately model dynamic topography and to avoid instabilities typically associated with free surfaces. The model also accounts for strain weakening where previously deformed materials are weaker than nondeformed materials. This allows for the simulation of faults and shear zones, because deformation will localize into weakened bands, which will become increasingly weaker and narrow (Buck & Lavier, 2001; Huismans & Beaumont, 2003). Strain weakening is justified for the plastic behavior of rocks due to a cohesion loss when the yield criteria is met. This loss in cohesion is associated with fault planes since they represent a discontinuity to the rock's integrity (e.g., Buck, 1993). Fluids penetrate faults from the surface, increasing the fluid pressure and also inducing mineral transformations, which together "soften" the effective friction angle (Bos & Spiers, 2002; Handy & Stünitz, 2002). Here, we choose to use only friction angle softening, because at depth cohesion contributes only a small amount to the yield stress in comparison to the friction coefficient that is multiplied by the pressure. Softening is applied as a linear function of the second invariant of finite plastic strain (Huismans & Beaumont, 2007), so that for no plastic deformation the friction angle is 30° and for finite plastic strain ≥1 the friction angle is 15°. Furthermore, we include viscous weakening with a linear increase in the pre-exponential factor of the dislocation creep law B (equation (8)). This represents weakening due to grain size reduction and crystallographic preferred orientation (Hansen et al., 2012; Karato & Wu, 1993). The viscous strain weakening rule chosen is such that the pre-exponential factor remains the same for no deformation and linearly increases with viscous deformation up to W_{max} times larger than the original value when the finite viscous strain is ≥1. This maximum weakening factor W_{max} is reduced in an Arrhenius-like fashion with temperature (T) to reduce weakening where crystal growth rates would be fast, with $W_{max} = 30$ when $T \leq 800\,°C$ and $W_{max} = 1$ when $T \geq 1200\,°C$ (Précigout & Gueydan, 2009; Ros et al., 2017).

Together, free surface and strain weakening allow for the simulation of faults and their associated relief, subsidence, and the elastic response of topography to tectonic and geomorphological loading and unloading. Consequently, the accommodation space for sedimentation and positive topographies for erosion are available, which is critical for this study.

2.1.1. Boundary Conditions and Initial Configuration

Initial model size is 400 km wide and 150 km deep. Half-extension velocities of 5 mm/year (ultraslow) are applied as lateral boundary conditions. For the bottom boundary we use a Winkler boundary condition (Buck & Poliakov, 1998; Burov & Poliakov, 2001), applying a constant upward stress at the bottom nodes. This stress corresponds to the basal lithostatic pressure at the beginning of the model run. This means we treat the base of the model as an unchanging level of isostatic compensation and allow for asthenosphere to flow in or out through the boundary. Thermal boundary conditions are 0 °C at the surface (including sediment surface) and 1300 °C below 120 km where heat transport is assumed to occur adiabatically by convection.

In our model, lithospheric and asthenospheric mantle share the same mesh layer. This means that the material properties in the mantle layer vary from dry olivine in the lithospheric mantle to wetter olivine in the asthenosphere (Table 1). The lithosphere-asthenosphere transition is placed at the initial model between 125 and 130 km depth (Hirth & Kohlstedt, 2003; Morgan, 1997; Morgan et al., 1995). This transition is tracked along time so that its position is known for every time step and the correct rheological parameters can be calculated for the mantle.

In addition, we impose a weak seed at the middle of the domain to nucleate rifting far from the lateral boundaries, avoiding boundary-related artifacts in the deformation. The weak seed is a region with the center located at 30 km depth where temperature is increased at the initial time step by 100 °C following a 2-D Gaussian function with half width 10×20 km. This increase in temperature makes viscosity smaller in that region. As the seed is allowed to thermally relax during the model run, it only helps to nucleate rifting and has a diminishing effect in later phases of rift evolution.

2.2. Sediment Transport Model

Topographic changes can be induced by both tectonic deformation and downslope transport of rocks along the surface toward areas of lower relief. For transport to happen, basement rocks need to loose their cohesion by transforming into sediment/regolith through erosion and weathering. Here, we assume that sediment is always available at the surface of the model and, consequently, that sediment transport dominates landscape evolution. We can therefore write that the change in surface elevation rate due to surface processes is equal to the divergence of the sediment flux, assuming there is no density difference between the bedrock and sediment and ignoring the effects of compaction. In 1-D this becomes

$$\frac{\partial h}{\partial t} = -\frac{\partial q_s}{\partial x}, \tag{10}$$

where h is the topography, t is time, q_s represents the sediment flux, and x is the horizontal coordinate (Culling, 1960; Smith & Bretherton, 1972). This implies that the temporal topographic variation for an element depends only on the difference between the input and output sediment fluxes for an element and, consequently, that landscape evolution is a function of spatial variations in sediment transport. This approximation is known as a transport-limited model (Dietrich et al., 2003; Howard, 1994; Kirkby, 1971; Kirkby & Carson, 1972). We chose this approach for our landscape evolution model since it allows for sedimentation to occur.

In the subaerial environment, it is possible to define the sediment transport flux q_s in terms of the water flux q_w as

$$q_s = -(K + c q_w^n)\frac{\partial h}{\partial x}, \tag{11}$$

where K is the slope diffusivity, c is the transport coefficient, and $n \geq 1$ is the power law that defines the type of relationship between the sediment transport and the water flux (Simpson & Schlunegger, 2003; Smith & Bretherton, 1972). This model accounts for hillslope diffusion processes where the topography will tend to a dispersive diffusion (Culling, 1960) and fluvial transport processes that result in concentrative diffusion due to water run off (Graf, 1984). For a simple parameterization we choose a linear relationship between sediment transport and water flux ($n = 1$).

The water flux can be related to the water discharge/effective rainfall α as

$$\frac{\partial}{\partial x}(\mathbf{n} q_w) = -\alpha, \tag{12}$$

where **n** is an unit vector directed down the surface gradient (Smith & Bretherton, 1972). By assuming a constant α and integrating equation (12) over the surface in the downstream direction, we obtain

$$q_w = \alpha x_d, \tag{13}$$

where x_d is the downstream distance from the drainage divide. By substituting equations (11) and (13) into (10) we obtain the 1-D sediment mass conservation equation for combined hillslope and discharge-dependent fluvial transport:

$$\frac{\partial h}{\partial t} = \frac{\partial}{\partial x}\left((K + k\alpha x_d)\frac{\partial h}{\partial x}\right), \tag{14}$$

where the downstream distance x_d is calculated at each time step as the distance from the topographic highs to the valley floors. Because q_w is dependent on the length of the drainage, the model mimics 1-D landscapes similar to river profiles in which fluvial processes are dominant.

In the submarine environment, sediment transport occurs in shallow waters due to the motion of waves and the tide. The intensity of these processes decreases with increasing water depth. This behavior can be reproduced by defining the sediment diffusivity as an exponentially decaying function of water depth (Kaufman et al., 1991):

$$\frac{\partial h}{\partial t} = \frac{\partial}{\partial x}\left(K_s e^{(-\lambda_s h_w)}\frac{\partial h}{\partial x}\right) \tag{15}$$

where K_s is the submarine diffusion coefficient, λ_s is the submarine diffusion decay coefficient, and h_w is the water depth (the difference between sea level and the submarine topography). Table 1 shows the sediment transport parameters used in equations (14) and (15).

We calculate the sea level with respect to the top reference surface of models by an isostatic balance, comparing to sea level for a 30-km-thick crust, which is a reasonable crustal thickness for continents with topography near sea level. Note that the initial top of our model is at 0 km, implying that sea level is below the model's 0-km reference topography.

2.3. Coupling of Tectonics and Surface Processes

Coupling between inner Earth dynamics and landscape evolution is done by first solving the tectonic model defined by equations (1)–(3) for a time step Δt, then advecting topography for Δt with the solved velocities and finally solving for sediment transport over the time step (equations (14) and (15)). This explicit approach implies that sediment transport during Δt occurs over a tectonically static topography that was previously calculated for the current time step. Therefore, this approach neglects the intra-time-step feedbacks between the load redistribution caused by the landscape model and the tectonic model. This approach is valid because the wavelength and amplitude of the topographic changes due to sediment transport are sufficiently small that their relaxation time is large compared with the size of the flow solver time step Δt (10 Kyr).

For numerical stability, we choose to run the sediment transport model for a number of smaller time steps Δt_s (1 Kyr) which in total sum to the tectonic time step Δt. Furthermore, the landscape evolution model mesh is adaptive so that high diffusivity contrasts at the interface between subaerial and submarine environments can be adequately resolved. Once the new topography is calculated from the sediment transport model, the y coordinates of the top nodes of the triangular grid are updated.

Variables for nodes and integration points of surface elements are resampled every time step after the topography update. In the case that nodes or integration points are located out of the old mesh due to sedimentation (see Figure S1), then their temperature is set to be the top boundary condition value (0 °C), their finite strain and rotated stress values are set to 0, and viscosity and strain rate (that are used in the next time step as initial guess for the nonlinear mechanical solver) are set to be the average of the closest element in order to ensure model stability. Thermal boundary conditions are set at the top boundary independently of the nature of the exposed rock (basement or sediment), and sediments are given the same thermal conductivity as the upper crust (Table 1).

In summary, the scheme used here for coupling the landscape evolution model to tectonics for a given time step Δt is as follows:

1. Run the flow and thermal solvers (tectonic model; equations (1)–(3)) for Δt, and obtain velocities, pressures, and temperatures.
2. Advect nodes with calculated velocities generating a new "tectonic topography."
3. Run the landscape evolution model for the new tectonic topography for i of Δt_s time steps, where $\Delta t_s = \Delta t/i$.
4. Update model topography with the final "landscape-model topography."
5. Resample variables for updated elements to match (and fill) this new top surface.

Ideally, sediments should have different mechanical properties and densities than those of the basement rocks. However, this would imply that the model includes an extra high-resolution discontinuous layer to represent sediments. The numerical resolution of this extra layer would need to be sufficiently high to have Delaunay triangles even when the sediment layer was as thin as a few meters (the case for the initial steps of the model). These extremely high resolutions are shunned because of the high computation time that would be spent in the Stokes flow solution step. Some strategies to reduce the number of small elements could be used, such as to only generate an independent sediment layer when the sediment thickness is on the scale of the resolution set for the crust (1 km). However, for simplicity, we choose to assume that the sediment's mechanical properties and density are crudely that of the upper crust (WQ, Table 1), and we simply include sediments into the upper crustal layer.

In terms of densities, this is analogous to maximum sediment compaction at the time of deposition. The implication of this is that the effects of sediment loading would be slightly diminished (a factor of $\frac{\sim 2,200 \quad \text{kg/m}^3}{2,700 \quad \text{kg/m}^3} \simeq 0.8$ to the topographic forces). Although this is not a realistic approach, we note that assigning lower densities to the sediments is also inaccurate as topographic diffusion preserves volume, therefore, different sediment densities will imply a decrease in total model mass. In order to preserve mass a more sophisticated landscape evolution model would be needed. However, we consider our simpler approach sufficient for this work as the difference between sediment and basement densities is minimal compared to the air-rock density contrast.

In terms of mechanics, this assumption is valid for shallow to intermediate depth sediments that deform in the elasto-plastic or brittle regime, since the effective viscosity is controlled by the yield criterion and not by the sediment's flow law parameters. However, deeper sediments at temperatures between 200 and 400 °C would be expected to deform by grain boundary diffusion creep driven by pressure solution (McClay, 1977; Rutter & Elliott, 1976). This deformation mechanism would result in larger strain rates for smaller stresses and, therefore, lower effective viscosities (Rutter & Elliott, 1976). Lower effective viscosities of the sediments could change details of deformation inside the sediment layer, potentially allowing for more distributed deformation within the sediment layer and detachment levels when viscosities are low. However, it is not in the scope of this work to accurately model sediment deformation during diagenesis. Instead, we focus on modeling the basement deformation that is affected by sediment loads and thermal blanketing. This is why we favor the simple mechanical characterization of sediment deformation that is chosen here.

3. Results

With the focus of better understanding how sedimentation affects margin architecture for different initial rheological profiles, we have run models in which we vary lower crustal rheologies, initial crustal thicknesses, and different fluvial transport coefficients. The set of models presented here is calculated over a parametric space that includes (1) a range in lower crustal rheologies (see Table 1), from strong to weak: GR, AN, and WQ (Gleason & Tullis, 1995; Hirth & Kohlstedt, 2003; Rybacki & Dresen, 2000; Wilks & Carter, 1990), (2) an initial crustal thickness of 35 or 40 km, (3) different fluvial transport coefficients ($c = 10^{-4}, 5 \times 10^{-4}, 10^{-3}, 5 \times 10^{-3}, 10^{-2}, 5 \times 10^{-2}$, including models with no SP), and (4) models with or without submarine surface transport processes. Combinations of these parameters led to a total of 78 experiments. The extension velocity is kept the same for all the experiments at 5 mm/year half-extension velocity. We will first describe the results of the models without SP in order to frame the interactions between SP and margin deformation (section 3.1). Then we discuss the results of models with SP, both at local and regional scales, with subaerial and submarine sedimentation (here called "Models with sea"), and with only subaerial sedimentation ("Models without sea"), in order to highlight the influence of marine inundation in comparison to models with sea (section 3.2).

3.1. Models Without Surface Processes

Results of models without SP have been extensively discussed in recent literature (i.e., Brune et al., 2014; Buck, 1991; Huismans & Beaumont, 2011; Ros et al., 2017; Svartman Dias et al., 2015). Here, these results are summarized to provide an overview of the different extensional modes observed and to frame the interactions between surface processes and margin deformation, that will be discussed in the following sections. For this purpose, we adopt the framework presented by Buck (1991) to characterize extensional modes. This approach allows us to describe the modeled margin geometry as the result of a succession of deformation phases, distinguishing distinct margin deformation domains. Among our models we can differentiate the three modes of rifting described by Buck (1991): (1) narrow (NR), (2) wide (WR), and (3) core complex (CC), plus (4) lateral rift migration (RM) through a low viscosity channel (Brune et al., 2014). Lateral rift migration generates asymmetric conjugate margins. When the LC is strong enough, lateral rift migration occurs in the upper crust as an array of sequentially active faults, which consistently young and dip oceanward (Pérez-Gussinyé, 2013; Ranero & Pérez-Gussinyé, 2010). Figure 1 exemplifies these rifting modes by showing the rift evolution of two models with 40 km crust, no SP, and different lower crustal rheologies: intermediate strength AN and weak WQ. Results with strong (GR) and intermediate (AN) lower crustal strength are very similar and are mainly discussed in the main paper in basis of the intermediate lower crustal results, for AN. Movies corresponding to the GR, AN, and WQ results are included in the supporting information.

Strong to intermediate lower crustal strength. Stronger LC models (GR and AN) typically begin with narrow extension and deformation localizing into two main faults that nucleate in the weak seed (Figure 1a and supporting information movies S1, S2, S7, and S8). This results in a central hanging wall block (also called the H-block by Lavier & Manatschal, 2006, or the keystone block by Huismans & Beaumont, 2011), which experiences large subsidence and thinning of the lower crust through shear zones. Once the lower crust has been attenuated, deformation moves into the central hanging wall block (Figure 1b). In models with initial 35-km crust, this phase typically ends with crustal breakup (S7 and S8 movies in supporting information). In the 40-km-crust models, the faults in the central block are accompanied by two outward-dipping shear bands which develop at the base of the crust (Figure 1b). These shear bands connect to various upper crustal faults dipping toward the center of the graben. Eventually, rift migration starts when one of the lower crustal shear zones becomes weaker due to strain weakening and accommodates more deformation than the other one. As deformation progresses in the favored shear zone, hot mantle upwelling, shear heating, and strain softening reduce the viscosity even further generating a lower crustal low-viscosity channel (LVC) that brings basal lower crust at the bottom of the LVC upward into the LVC foot-wall (see velocity arrows in Figure 1c) as described by Brune et al. (2014). At this stage several faults dipping both inward and outward detach into the LVC. Subsequently, the sequential faulting mode begins when one of the upper crustal faults starts to dominate deformation and couples with the favored lower crustal outward-dipping shear band or LVC (Figure 1d and section 3.2.3). Note that in the models, sequential faulting does not necessarily occur through a single fault at a time. Instead, up to two faults can be simultaneously active dipping oceanward together with an antithetic fault located in the narrow margin. In models, the sequential faulting phase finishes due to cooling of the upwelled mantle and consequent strengthening of the lower crustal shear band (Brune et al., 2014). The 40-km-crust models finally reach crustal breakup by localization of brittle deformation into the thinnest sector of the asymmetrically thinned crust.

Weak lower crustal strength. In these experiments the initial extensional phase occurs by wide rifting mode. Extension is distributed through a wide region (~200 km) at the center of the model, but faults located above the weak seed accommodate most of the deformation (Figures 1e and S3 and S9 movies in the supporting information). In these models, the shallowest portions of the upper crust deform in the brittle regime while the lower crust is viscous and very weak. These conditions favor lower crustal flow toward the area of upper crustal extension that inhibits crustal thinning and results in a switch in rifting mode, from wide rifting to core complex mode (Figure 1f). As extension progresses and the availability of low viscosity lower crust to feed the CC decreases, the CC die out and deformation moves out of the basin center to concentrate in the outward-dipping shear zones and their linking upper crustal faults (time steps 8 and 11 Myr in S3 and S9 movies in the supporting information). With time, the mantle keeps rising at the center, further weakening this region so that deformation jumps again into the area of the abandoned CC (Figure 1g and time steps 11 and 14 in S3 and S9 movies in the supporting information). In models with initial 35-km crust, breakup occurs in that area after a short phase of deformation, resulting in two symmetric conjugate margins
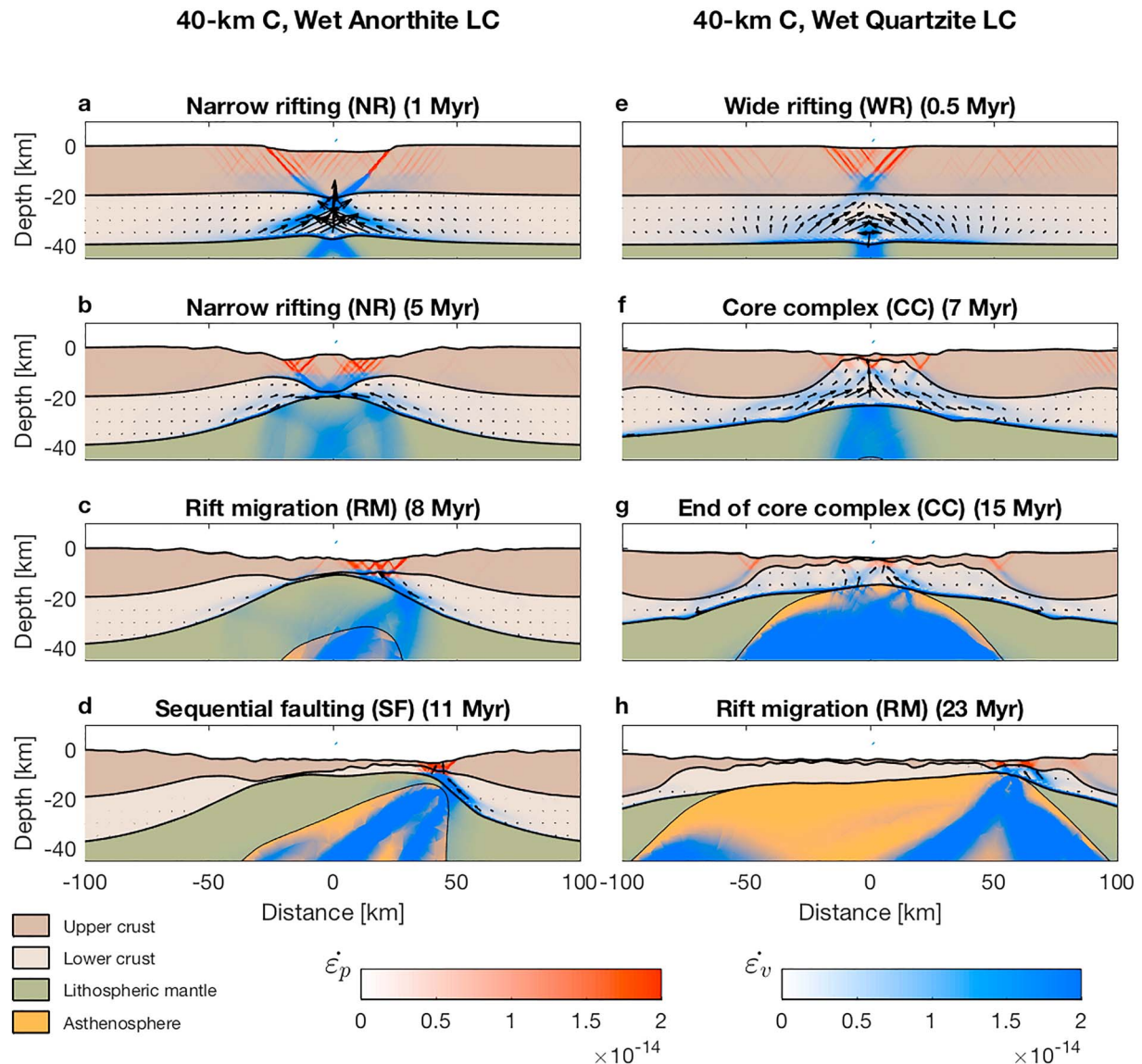
Figure 1. Rifting evolution and extensional modes of models with wet anorthite (a–c) and wet quartzite (d–f) lower crustal rheologies and initial crustal thickness of 40 km. Arrows represent relative-to-surface lower crustal velocities calculated for the given time step. Red and blue colors represent plastic ($\dot{\varepsilon}_p$) and viscous ($\dot{\varepsilon}_v$) second invariants of the strain rates, respectively, $[s^{-1}]$, which are representative of the amount of plastic and viscous deformations occurring at the given time step. LC = lower crust.

(Figure 6a and Figure S7). In models with initial 40-km crust, one of the outward-dipping LC shear zones becomes dominant and produces rift migration toward one side of the system. In this case, the LVC is wider and dips at a lower angle than in the stronger models. Consequently, faults rooting at the migrating LVC are distributed over a wider area, are more numerous, and have smaller offsets than in the stronger models. Although lateral rift migration is active from 18 Myr, sequential faulting in the upper crust only begins much later (from 24 Myr, supporting information S3 movie). As in the stronger models, breakup occurs when cooling leads to the vanishing of the LVC. The final geometry consists of two highly asymmetric conjugate margins, where the widest margin is ∼240 km and the narrowest ∼40 km wide (Figure 8a). Note that these models create lower amplitude relief than stronger ones due to their more distributed deformation associated with weaker lower crust and faster viscous relaxation times.

3.2. Models With Surface Processes
In this section we first discuss the general implications of erosion and sedimentation under extension at the local scale (sections 3.2.1–3.2.3), and then address effects of SP on regional margin architecture (section 3.2.4).
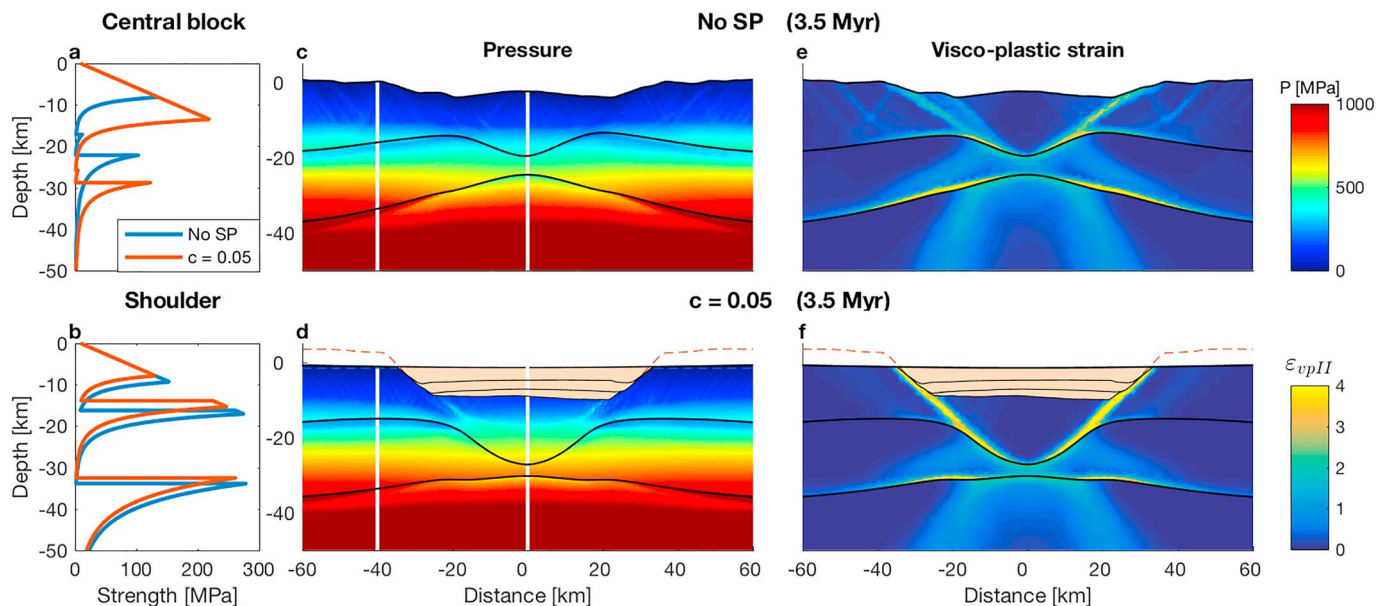
Figure 2. Impacts of surface processes in pressure and strain localization. Strength profiles of a model with no SP and a model with SP ($c = 5 \times 10^{-2}$) are shown in (a) for the central block and in (b) for the rift shoulder. Panels (c) and (d) show pressures (P) for a model with no SP and a model with efficient subaerial SP with fluvial transport coefficient $c = 5 \times 10^{-2}$, respectively. Panels (e) and (f) show second invariant of the visco-plastic strain for both no SP and $c = 5 \times 10^{-2}$ models, respectively. Sediments are colored in light brown, and black lines inside the sediments represent depositional time lines at 1 Myr time intervals. The vertical white lines in (c) and (d) indicate the locations of the strength profiles (a, b). Pressures at the central block are larger in the model with SP (d) than in the model with no SP (c), due to sediment loading. This forcing effect results in larger displacement and fast weakening at the initial faults that leads to strain localization (f vs e). SP = surface processes.

3.2.1. Effects on Pressure, Crustal Strength, and Faulting

In agreement with previous work (e.g., Olive et al., 2014; Zwaan et al., 2018), an increase in the efficiency of surface processes promotes strain localization in the brittle regime. Figure 2 represents the initial faulting phase for a model with no SP (Figures 2a, 2c, and 2e) and efficient SP (Figures 2b, 2d, and 2f). Erosion at the uplifting foot-wall reduces vertical forces at this location, allowing for further uplift (Olive et al., 2014), and prevents fault and foot-wall rotation (Zwaan et al., 2018; Figure 2). Sedimentation occurs in subsiding hanging walls, which increases pressures at the upper crust (Figures 2c and 2d, center of the plot). The increase in the difference between foot- and hanging wall pressures results in larger displacements along faults for a given period of time, with larger accumulated deformations, fault weakening, and deformation localization in the case of efficient SP. This means that in models with efficient SP, deformation can be accommodated on only two main faults (Figure 2d), while several faults act simultaneously in the no SP model (Figure 2c). Furthermore, the addition of sediments on top of the hanging walls leads to an increase of the upper crustal strength (Figure 2a) which prevents faulting of the subsiding crustal block. In the no SP model, faults rooting at the base of the upper crust, into a viscous channel, occur outward from the initial two main faults (Figure 2e). When erosion is active, the consequent thinning of the upper crust leads to a thinning of this viscous channel (Figures 2b and 2f) and, therefore, diminishing the ability of faults to occur outward from the initial faults. The combination of all these factors leads to faults remaining active for a longer period of time, with larger total deformation along them when SP are efficient. When brittle deformation is the dominant extension mechanism, efficient SP lead to an increase in fault offsets, foot-wall uplift, and hanging wall subsidence, a reduction in the number of faults and, consequently, significant changes to the margin structure.

3.2.2. Effects on Temperature and Ductile Deformation

As for brittle deformation, efficient surface processes enhance localization of deformation in the viscous regime due to their effect on reducing the topographic forcing against fault displacement. However, when the sediment thickness is large enough, the thermal blanketing effect of sediments and the greater depth of the basement leads to greater temperatures (Theissen & Rüpke, 2010). This reduces viscosities due to temperature dependence of the flow law (equation (8)) and, therefore, favors ductile over brittle deformation, even in the upper crust (Figure 3). The thermal blanketing effect is greater for weaker rheologies as lower viscosities occur for the same temperatures, preventing rocks to reach their yield stress.
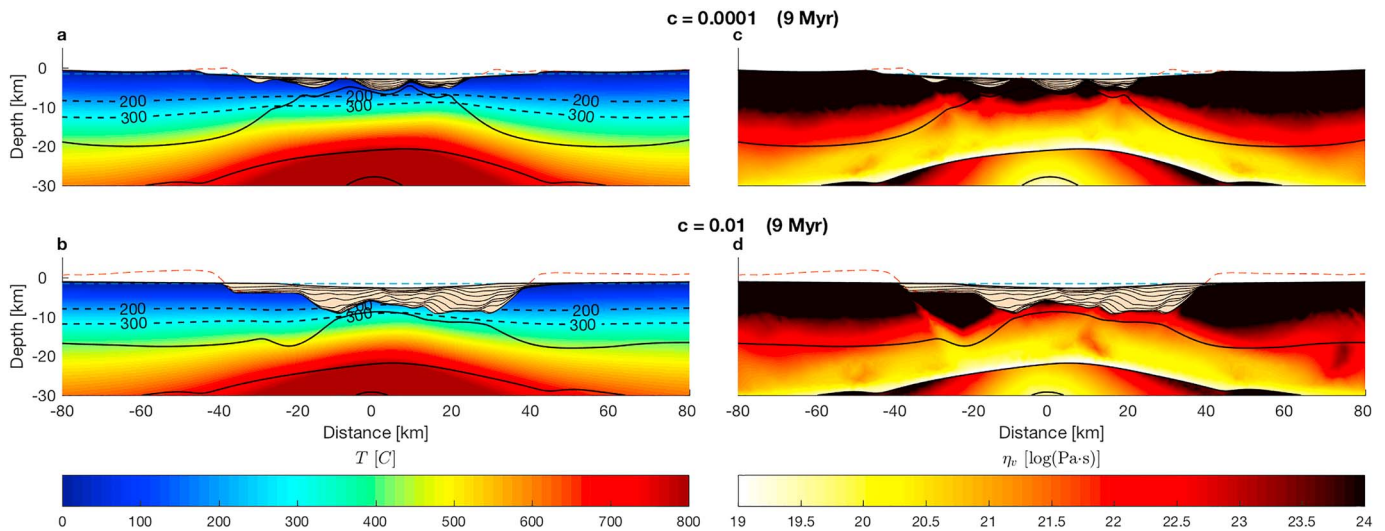
Figure 3. Sediment thermal blanketing and effects on viscosity. Panels (a) and (b) show temperature fields of 40-km crust wet quartzite models with less efficient surface processes ($c = 10^{-4}$) and more efficient surface processes ($c = 10^{-2}$), respectively. Dashed black lines represent isotherms of 200 and 300 °C. Panels (c) and (d) show correspondent viscous fields. Dashed blue lines mark the sea level. Light brown color represent sediments and black lines are depositional time lines for a 1 Myr time interval. Note that, in the central region of (b), upper crustal temperatures are between 200 and 300 °C, while in (a) upper crust temperatures in the central region are below 200 °C. Also, the thermal gradient at the center of (b) is larger than in (a). This difference in crustal temperatures and gradients is the result of thicker sediments in (b) that exert a significant blanketing effect on basal temperatures. This decreases upper crust and lower crust viscosities in (d). Note that sediments are taken into account when calculating the temperature field, but their temperature is not shown in this figure.

3.2.3. Feedbacks Between Loading, Thermal Blanketing, and Rift Migration

Lateral rift migration produces conjugate margin asymmetry in the models. As previously described, the underlying mechanism for RM is the presence of an outward-dipping dominant channel/shear zone of low viscosity (LVC) at the base of the lower crust. The LVC focuses extension to one side of the upwelling mantle dome and connects deformation in the upper crust, lower crust, and mantle. Asymmetric upwelling of the hot mantle toward the LVC weakens the shear zone's hanging wall and forces migration of the deformation toward this area, leading to lateral rift migration. As the LVC migrates, new faults develop in its hanging wall and root into this shear zone. Therefore, this mode is highly dependent on both plastic and viscous deformation, and it is sensitive to the effects of sediment loading and thermal blanketing. Additionally, this mode takes place during later stages of rifting where basins are already deep, and where available sediment is likely to be scarce (i.e., submarine basins).

Figure 4 exemplifies the potential feedbacks between sediment loading and thermal blanketing on lateral rift migration for models with AN lower crust, 40-km initial crustal thickness and different SP efficiencies ($c = 5 \times 10^{-3}$, 10^{-2} in Figures 4e–4l) and subaerial as well as submarine SP (i.e., models with sea). For comparison, models without surface processes are also shown (no SP in Figures 4a–4d). At 8 Myr, the LVC on the right hand side of the models has just become dominant over the left hand side one (Figures 4a, 4e, 4i, and S2 and S10 movies in the supporting information). However, sequential faulting in the upper crust has not yet started. Instead, a group of faults both dipping oceanward and landward accommodate extension on top of the LVC in all models (Figures 4a, 4e, and 4i). In the model with no SP, sequential faulting starts at 10 Myr (Figure 4b) in contrast with models with SP in which sequential faulting is delayed (Figures 4f and 4j). The delay in the onset of sequential faulting occurs because increasing sediment thickness at the LVC hanging wall leads to larger offsets at LVC antithetic faults (e.g., f0, f1, and f2 in Figures 4e, 4f, 4i, and 4j) and associated crustal subsidence. This reduces the dip of the LVC (compare dip of LVC in Figures 4b and 4j). Additionally, increasing sediment thickness increases crustal temperatures which allows the LVC to continue to deform at low angles and also at the base of the upper crust (see ductile domains at the base of the upper crust in Figures 4e–4g and 4i–4k). Consequently, in models with increasing SP the LVC works as a gently dipping, low viscosity crustal level in which a group of faults detaches, which delays the start of sequential faulting. With increasing extension, deformation also localizes in the $c = 5 \times 10^{-3}$ model, leading to sequential faulting (Figure 4g). At later stages of the model with the largest sediment thickness, crustal
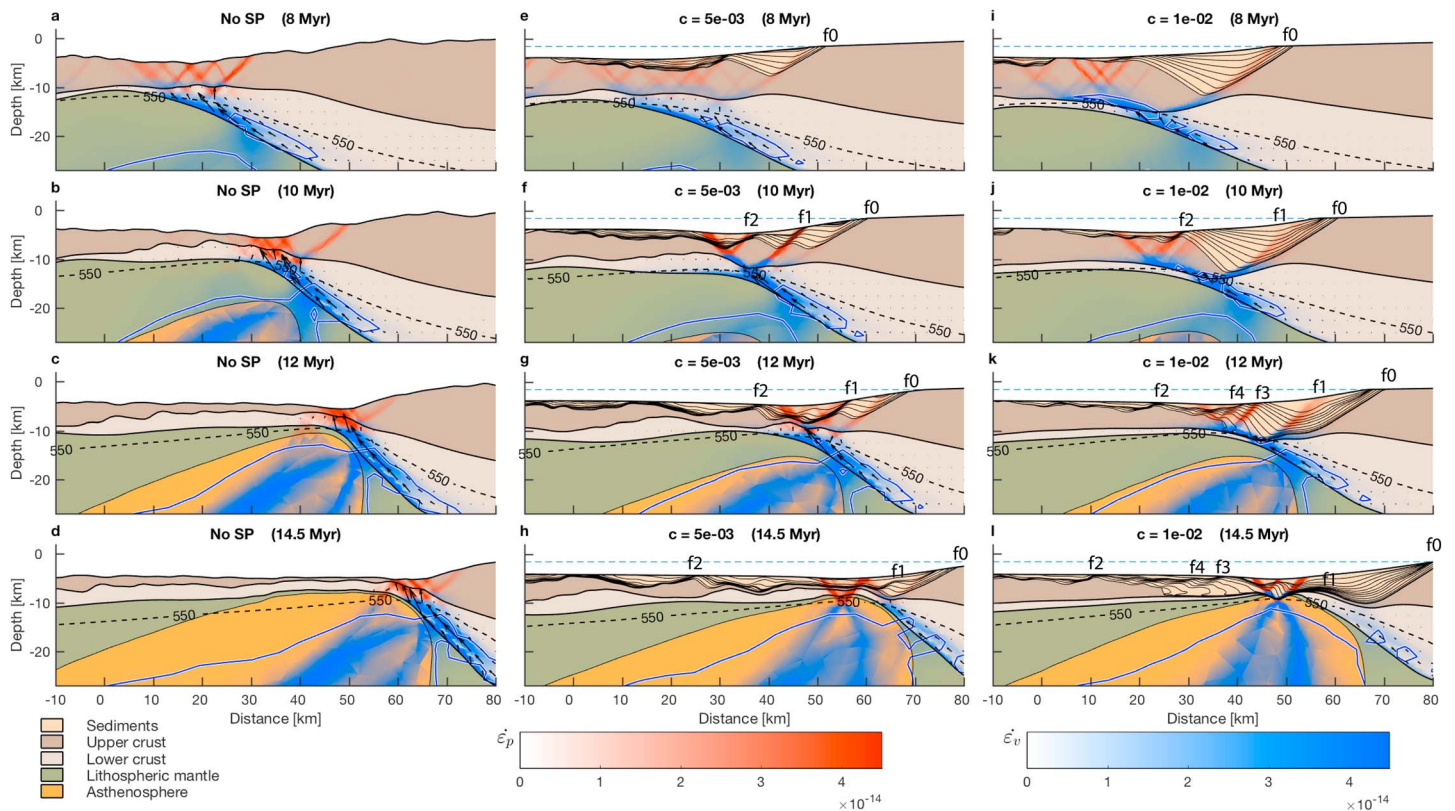
Figure 4. Rift migration for wet anorthite models with 40-km initial crust under different SP efficiencies. Panels (a)–(d) represent the evolution of a model without surface processes, (e)–(h) with SP and $c = 5 \times 10^{-3}$, and (i)–(l) $c = 10^{-2}$ and subaerial as well as marine sedimentation. Black lines inside the sediments represent depositional time lines at 1 Myr time intervals. Black arrows represent velocities of the lower crust relative to the upper crust. Red and blue colors represent plastic ($\dot{\varepsilon}_p$) and viscous ($\dot{\varepsilon}_v$) strain rates, respectively. The dashed blue line in (e)–(l) marks the sea level. The continuous blue line is the $10^{20.5}$ Pa·s viscosity isoline. f0 to f4 are faults which are antithetic to the low viscosity channel and formed in its hanging wall, in the narrow conjugate side during extension. Note for increasing c, the dip of the low viscosity channel decreases and faults f0–f4 have larger offsets. Also note that some of these faults are later incorporated into the final wide margin (faults f2–f4 in (f)–(h) and (j)–(l)) together with allochtone sediments, due to rift migration. SP = surface processes.

extension occurs solely by viscous deformation in the crust with several brittle faults in the sediments, which are antithetic to the LVC (f1, f3, and f4 in Figure 4k).

Breakup occurs earlier and is closer to the model center in models with greater SP efficiencies (Figures 4d, 4h, and 4l). This is a consequence of antithetic faults located in the hanging wall of the migrating LVC, which are more active in thinning the hanging wall under increasing sedimentation. Note that these faults are active in the basement and sedimentary sequences and become part of the future wide margin (e.g., faults f2, f3, and f4 in Figures 4f–4h and 4j–4l). Thus, the final wide margin contains both oceanward dipping faults, which formed with the same dip as the LVC shear zone, as suggested in the sequential faulting model (Ranero & Pérez-Gussinyé, 2010), and landward dipping faults induced by sediment loading of the narrow margin. These latter faults bring sediments outsourced from the narrow margin into the wide margin. For the model with the largest subaerial transport coefficient ($c = 10^{-2}$), large sedimentation in the future narrow margin, induces long offset antithetic faults (f0, f1, f3, and f4 in Figures 4j and 4k). These faults, combined with ductile deformation of the upper crust in the last stages of extension, break apart the upper crust and juxtapose lower crust and sediment at the distal part of the wide margin at breakup (Figures 4k, km 35–60, and 4l, km 27–49).

For models with only subaerial SP there is relatively efficient erosion and sediment delivery to the area of active deformation (Figure S27). This results in greater flattening of the dominant shear zone and an increase in the amount of ductile deformation in the upper crust that postpones the onset of sequential faulting. In cases with efficient sediment transport, large piles of sediments in the model center result in longer-lived deformation at this location, ductile deformation within most of the upper crust, and a final symmetric conjugate margin pair.
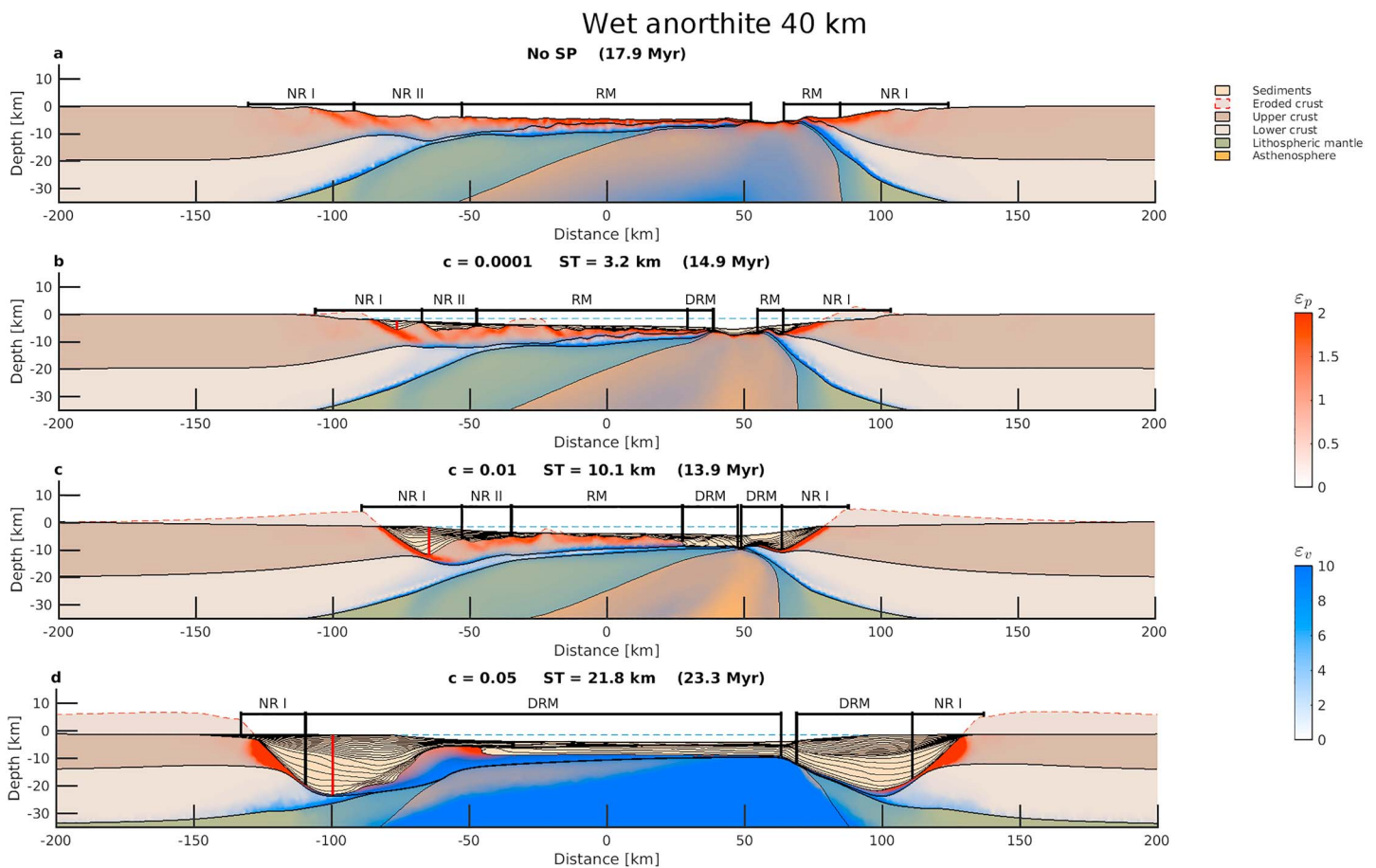
Figure 5. Margin geometry after crustal breakup for a 40-km initial crustal thickness and wet anorthite lower crust. (a) Model without SP and (b–d) models with different subaerial transport coefficient ($c = 10^{-4}, 10^{-2}, 5 \times 10^{-2}$). Red and blue shadows represent plastic (ε_p) and viscous (ε_v) finite strain (total deformation), respectively. Black lines inside the sediments mark 1-Myr spaced time lines. Margins are divided into deformation domains (section 3.2.4). Vertical red lines represent the maximum ST across the profiles, quantified in each subfigure tittle. Discontinuous blue line marks the sea level. SP = surface processes; ST = sediment thickness; NR I = initial narrow rifting domain; NR II = narrow rifting domain II; RM = rift migration; DRM = ductile rift migration.

For weak crustal rheologies (WQ), and models with sea, rift migration also takes place through a LVC, but LVC angle is lower and faulting is more distributed than in the cases with stronger rheologies (Figures S28 and S3 movie). As in the previous described cases, an increase in sediment thickness increases the importance of ductile deformation within the lower and upper crust. In cases with very efficient SP, ductile deformation in the basement is so dominant in the narrow margin that brittle deformation in the sediments is very distributed, with clear faults indiscernible at this scale/resolution. If an actual margin would have undergone this type of extension, its seismic section would image pervasive short-offset faulting in the sediments over a nonstructured basement. Syn-rift sequences in the narrow margin would also appear post-rift.

3.2.4. Effects on Regional Margin Architecture

In order to evaluate the contribution of the different rifting modes to the final margin architecture and the effect of surface processes into these extensional modes, we identify different crustal deformation domains for each margin. These deformation domains represent margin sectors in which the last deformation phase in the crust occurs by one of the extensional modes previously defined in section 3.1, plus some additional deformation scenarios observed in the models with sedimentation. We define eight possible domains: (1) initial narrow rifting domain (NR I); (2) narrow rifting domain II (NR II), associated with the extension of the central hanging crustal block or keystone; (3) wide rifting; (WR) (4) core complex domain (CC); and (5) rift migration domain (RM) in which upper crustal deformation is mainly brittle. In addition we can observe (6) a ductile rift migration domain (DRM) in which the last extension phase leads to rift migration accommodated only by ductile deformation in both upper and lower crust; (7) a ductile pure-shear domain (DPS) in
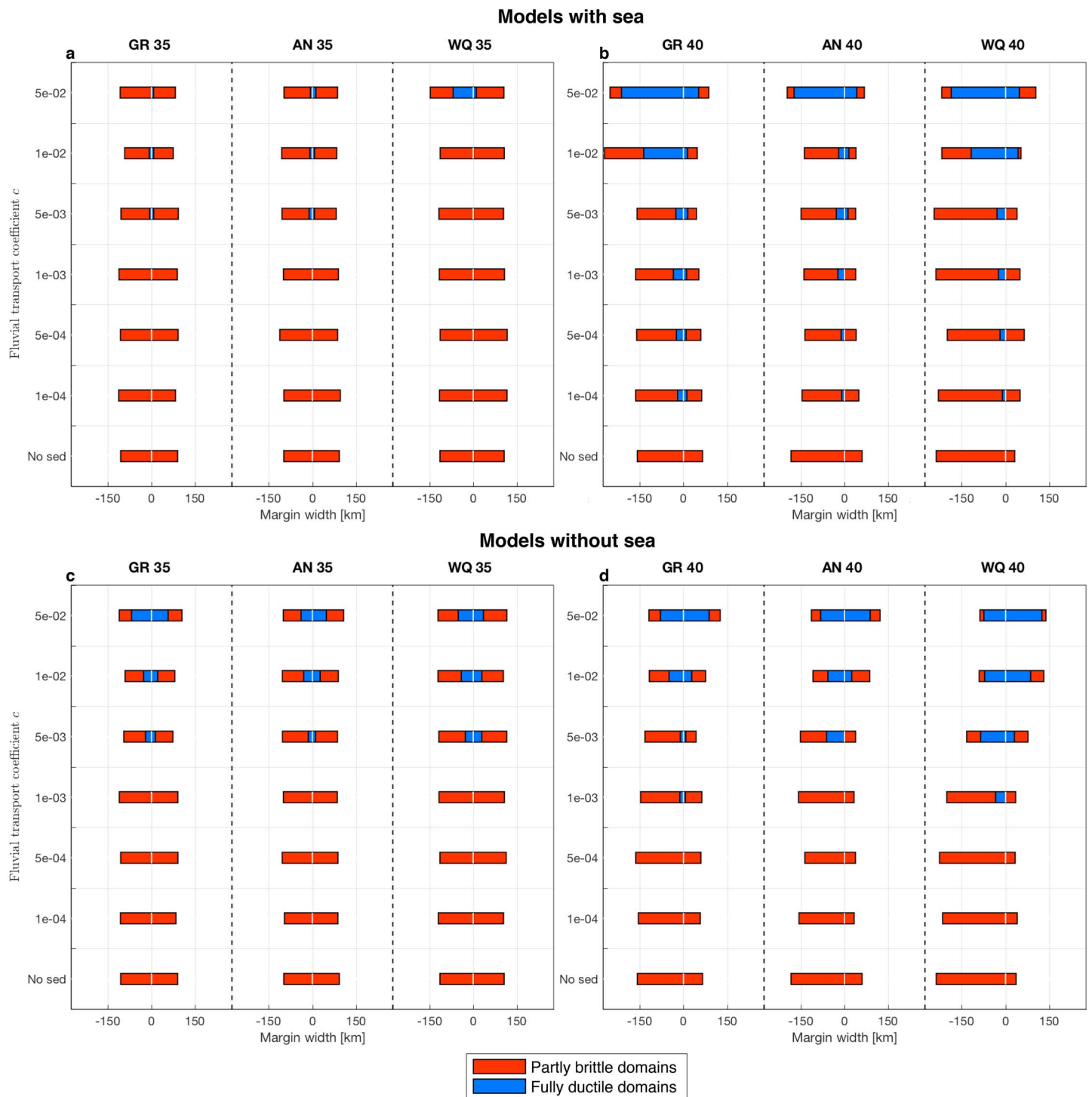
Models with sea

Models without sea

Partly brittle domains
Fully ductile domains

Figure 6. Margin width of models with sea. In (a) margins calculated for initial 35-km crustal thickness, and (b) for 40-km. The white line at 0 represents the crustal breakup, and red and blue stand for partly brittle B and fully ductile D domain widths. Increasing subaerial sediment transport coefficient increases D domain widths. GR = lower crustal rheologies mafic granulite; AN = wet anorthite; WQ = wet quartzite.
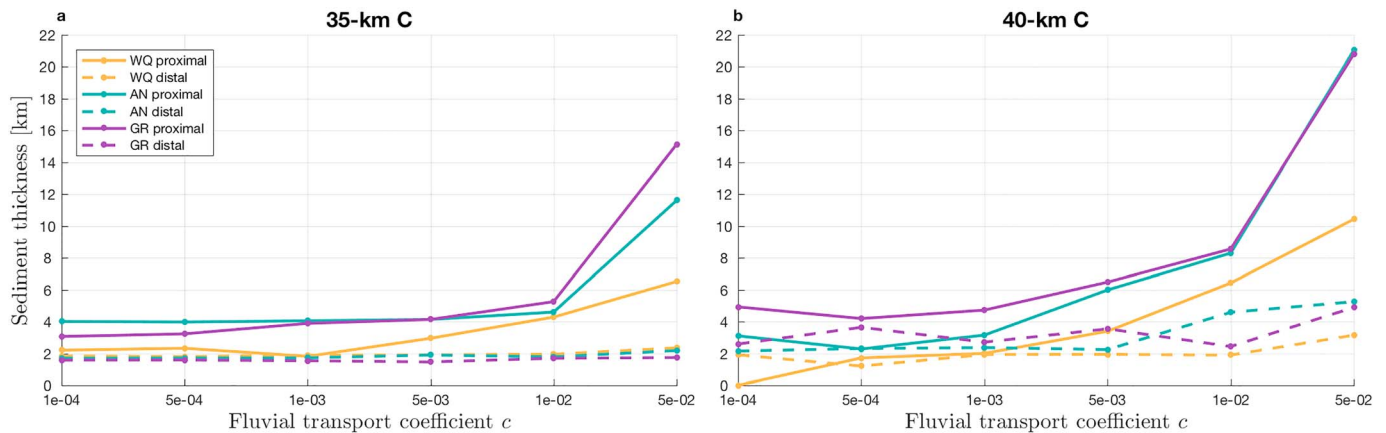
Figure 7. Sediment thickness versus fluvial transport coefficient for different rheologies and initial crustal thickness. Data labeled as proximal represent an average of sediment thickness measured at the basin depocenters closest to the main initial fault at each of the two conjugate margins. Data labeled as distal represent the sediment thickness overlaying the first mantle exhumed after breakup. Note that sediment column is thinner for WQ margins in the proximal sectors of the margins due to smoother topographies related to the extension of a weaker crust. GR = lower crustal rheologies mafic granulite; AN = wet anorthite; WQ = wet quartzite.

which the last extension phase occurs in a pure-shear manner by ductile mechanism in the upper and lower crust; and (8) a shoulder collapse domain (SC) in which a rift shoulder subsides due to lower crustal flow outward from the shoulder into or out of the margin. We examine the different extensional modes during rift evolution in order to identify the crustal deformation domains (see movies in the supporting information). The extension mode at these crustal domains and their width depends on the crustal rheology, the thermal state, the rifting history, and the efficiency of SP. Note that, with the exception of the ductile domains, all domains deform in part brittly. Consequently, we will refer to all these domains as partly brittle domains (B) and to the ductile domains as fully ductile (D). The total widths of domains that have deformed partly brittly and those in which the last deformation phase was fully ductile are shown in Figure 6, as a proxy for the effect of SP in plastic/viscous deformation. The different areas that underwent the previously described deformation modes for the models with 40 km initial crustal thickness, and anorthite and wet quartzite LC, are shown in Figures 5 and 8. Corresponding figures for the rest of the models are shown in the supporting information (Figures S3–S26).

Models with sea. At the start of extension, all model topography is above sea level and experiences sediment transport by subaerial processes during the first phase of rifting. Once deformation localizes, effective subsidence of the hanging block results in the ocean filling the graben basin, and a change in depositional environment from subaerial to submarine: shallow sediments near the coast are transported efficiently into the shelf while sediment transport is less efficient in the deep sea. Consequently, the effects of SP on extension mechanisms depend on whether deformation takes place on the shelf or in deeper portions of the new sea, to which less sediment can be transported (equation (15)).

In stronger LC models (GR and AN) and 35-km initial crust, an increase in subaerial transport coefficient c results in larger inflow of sediments into the proximal domains NR I and II, and increasing erosion of the rift shoulder (Figures S3–S6 and S4, S6, S7, and S8 movies). This leads to a slight reduction in the width of domains NR I and II and a reduction of the partly brittle domains, with increasing c (Figure 6a) through sediment loading effects (see section 3.2.1). Small fully ductile domains (DPS) appear for large c as the result of thermal blanketing in combination with hot mantle upwelling. The increase in length of the domains behaving fully ductile compensates for the decrease in length of the domains behaving partly brittly, so that the total width of margins remains fairly constant with increasing sediment thickness, that is, increasing c (Figure 6a).

With increasing SP efficiency, the stronger models (GR and AN) with 40 km initial crust also suffer a reduction in the width of partly brittle domains, in particular domains NR I and II and the RM domain (see Figures 5 and 6b and Supporting Information Figures S9-S12). While NR I and NR II, become narrower due to sediment loading effects, the length of the RM domain decreases due to an increase in ductility related to thermal insulation by sedimentation and mantle upwelling. This induces a switch to ductile rift migra-
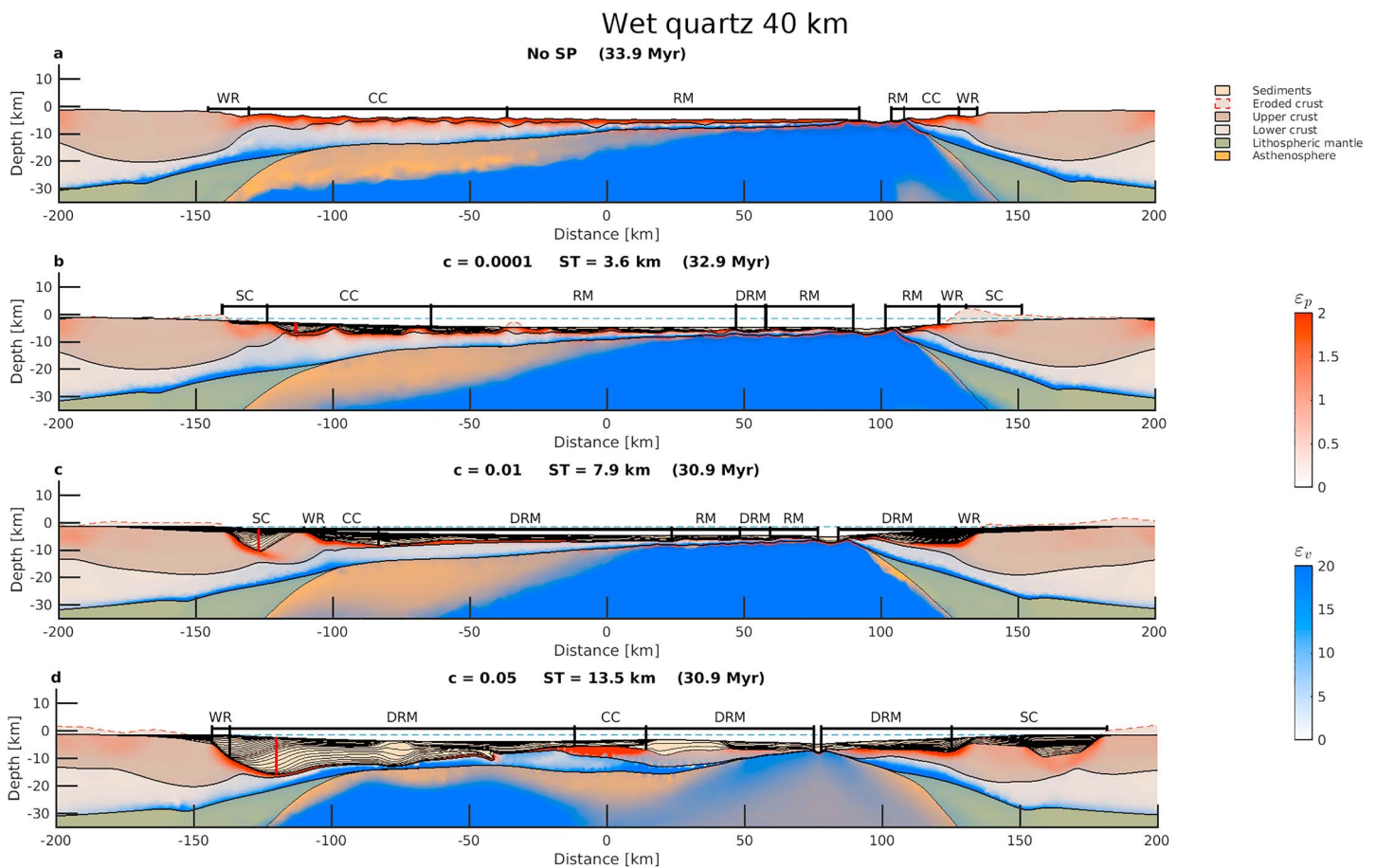
Figure 8. Margin geometry after crustal breakup for a 40-km initial crustal thickness and wet quartzite lower crust. (a) model without SP and (b–d) models with different subaerial transport coefficient ($c = 10^{-4}, 10^{-2}, 5 \times 10^{-2}$). Red and blue shadows represent plastic (ε_p) and viscous (ε_v) finite strain (total deformation), respectively. Black lines inside the sediments mark 1-Myr spaced time lines. Margins are divided into deformation domains (section 3.2.4). Vertical red lines represent the maximum ST across the profiles, quantified in each subfigure tittle. Discontinuous blue line marks the sea level. Note that outboard basins associated to the initial WR phase are not included in the deformation domains of this models (see S3 movies in the supporting information) since we focus on the central basin which accommodates most of the extension. SP = surface processes; ST = sediment thickness; WR = wide rifting; CC = core complex; RM = rift migration; DRM = ductile rift migration; SC = shoulder collapse.

tion in the last phases of extension (supporting information movies S1, S2, S10, and S12). The total margin width only changes significantly for $c \leq 10^{-2}$, where widening of ductile domains results in wider margins (Figures 5d and 6b). Note that the degree of symmetry/asymmetry of conjugate margins is not affected by SP when sea is present (Figure 6b).

In weak models (WQ) smoother topographies develop than in stronger models, since deformation is more distributed and LC flow produces rapid relaxation of sharp relief. As erosion depends on slope (equations (14) and (15)), the proximal areas of weak rheology models have lower sediment thickness than strong ones for the same c coefficients (Figure 7). However, distal regions show little variation in sediment thickness for different c, because of the large reduction in sediment transport in marine environments (Figure 7). Consequently, increasing c in 35-km WQ models only affects the widths of proximal domains, which partly deform brittly when $c \leq 10^{-2}$ (B domains in WQ Figure 6a and WR, CC, and RM in Figure S8). For the same reason, the fully ductile domain D is only present in the 35-km model with $c = 5 \times 10^{-2}$ (Figure 6a).

In weak models with initial 40-km crust, conjugate margin asymmetry occurs through a final phase of rift migration (Figure 8 and movies in the supporting information S3 and S11). Again, slow sedimentation rates in the marine basins result in small effects on width reduction in brittle domains and increase in ductile domain width when $c < 10^{-2}$ (Figures 6b). However, for a given proximal sediment thickness (i.e., ~6.5 km in WQ $c = 10^{-2}$, Figure 7b) D domains in GR and AN models of similar thickness ($c = 5 \times 10^{-3}$ for GR and

AN, Figure 7b) are narrower (~50 GR and AN vs ~150 km in WQ Figure 6b). We conclude that weaker lower crust is more sensitive to the effects of thermal blanketing. Note that there is also a considerable reduction in margin asymmetry for $c = 5 \times 10^{-2}$ (Figure 8d). In this case, it is due to the suppression of the rift migration phase, with its substitution by several fully ductile rift migration phases in which deformation is less localized and several rift jumps occur (Figure 8d and S11 movie in supporting information).

Models without sea. Extension typically occurs in regions with deep relief. If these deep topographies are not covered by water, only subaerial SP are present during extension. This is important because subaerial SP are more efficient in transporting sediments into the deepest topographies and areas undergoing deformation than are submarine ones. In this section, we present models with only subaerial processes, as an end member for high sediment transport into the distal margin domains.

In this case, 35-km models showcase symmetric conjugate margins for all values of c and all rheologies considered (Figure 6c and Figures S15–S20 and 35-km movies). Reduction of B domain widths (NR I and II) is observed for $c \geq 10^{-3}$ (Figure 6c). D domains are present in models in which $c \geq 10^{-3}$ and their widths increase with increasing c. However, margin length does not change with increasing SP efficiency (Figure 6c) because increasing in D domain widths compensate for the decrease in B width, as also observed in 35-km models with sea.

Models with initial 40-km crustal thickness showcase a larger decrease in B domain widths (NR I, II, and RM) and a larger increase in D domains, with increasing c, in comparison to models with sea (Figure 6d and Figures S21–S26 and 40-km movies). The larger decrease in B width is justified as more sediments deposit on tectonically active sectors across the full rifting history, enhancing strain localization at faults. The increase in ductile domain widths is associated with thermal blanketing effects that reduce, overprint, and/or suppress NR II and RM (Figure 6d and Figures S21–S26). However, in this case, for $c \geq 10^{-2}$ D domains do not occur by rift migration. Instead, conjugate ductile domains deform simultaneously by pure shear extension (DPS in Figures S21–S26 and S14, S15, S17, S18, S21, and S24 movies). This occurs because a high degree of brittle strain localization takes place during initial rifting phases, penalizing rift migration (see section 3.2.3) and leading to a more symmetric setup for later rifting phases (see Figure S27k). High sediment thicknesses in distal basins (i.e., thermal blanketing) favors pure shear viscous deformation in the center of the model during later rifting phases. The ultimate impact on margin geometry of the absence of a sea is therefore a substitution of rift migration domains (RM and DRM) by symmetric ductile pure-shear domains (DPS) with very attenuated crust, leading to symmetric conjugate margins (Figure 6d).

4. Discussion

4.1. New Insights in the Effects of Surface Processes on Rift Development

Our study shows that surface processes have important consequences for the modes of deformation and final architecture of margins. This influence is more obvious with increasing efficiency of surface processes. Because subaerial SP are more efficient than submarine ones, the proximal areas of margins where subaerial SP are more likely to take place are more obviously affected than the submerged distal sectors. In particular, we observe that, during the first phases of rifting, high erosion and sedimentation rates at the foot- and hanging walls, respectively, facilitate displacement on faults. This occurs because topographic and flexural forces opposing slip through an existing fault are reduced by surface processes (Buiter et al., 2008; Burov & Poliakov, 2001; Olive et al., 2014). Owing to this, the increasing efficiency of SP during the initial phases of rifting result in (1) localization of deformation in fewer, larger-offset, and longer-lived faults which can prevent deformation to spread out into the rift shoulders, (2) an increase in fault spacing and fault-block size, (3) a longer-lived narrow rifting phase, and (4) a more symmetric setup of the crustal structure at the end of this initial phase of extension. At the regional scale, a direct consequence of these effects is that domains formed during early stages of rifting (controlled by plastic deformation) under subaerial or shallow marine environments would be narrower and their fault offsets would be larger with increasing subaerial SP efficiency, due to strain localization. This is in agreement with previous analytical, numerical, and analog model results (Allen & Beaumont, 2016; Bialas & Buck, 2009; Buiter et al., 2008; Burov & Poliakov, 2001; Olive et al., 2014; Zwaan et al., 2018). However, those works, with the exception of Allen and Beaumont (2016) which focuses on salt deposition, use simpler setups that lack nonlinear and/or temperature-dependent viscosities in the LC, or lack elasticity and/or a realistic landscape evolution model (e.g., that lack erosion and basin-filling occurs to a fixed base level). This hinders understanding of the effects of marine incursion into the rift area

and of how sedimentation affects the deformation mode and basement structuring throughout the rifting history, including effects on the distal margins.

Our new findings are particularly relevant for the effects of marine incursion and the structuring of distal regions of margins. When submarine as well as subaerial SP take place (models with sea), we see no clear change in conjugate margin symmetry (Figures 6a and 6b). However, we do see a change in the structure of the basement. Here, thermal blanketing leads to a switch from plastic (i.e., deformation by faulting) to viscous deformation, even in the upper crust, at later rifting stages. This is reflected in a distal area where the basement lacks fault-block structure (i.e., an unstructured basement) and its width increases with the efficiency of SP (DRM in Figures 5 and 8). These attenuated unstructured crustal domains are dominated by ductile deformation of the entire crust.

When submarine SP are not present (models without sea), sediment input into the distal margins is larger and may lead to a change in the original symmetry of the conjugate margins. For example, while margins that were originally symmetric stay symmetric (Figure 6c), those that were originally asymmetric without SP may become symmetric given enough sediment input (Figure 6d). This increase in the symmetry of the conjugate margins is due to the fact that large sediment input into the deep basin results in larger localization of deformation on faults at the center of the model, combined with later thermal insulation and predominance of pure shear ductile deformation (Figure 6d). This points out at the importance of changes in sedimentation environments for the conjugate margin symmetry/asymmetry (i.e., a late marine incursion favors symmetry in contrast to an early sea incursion, Figure 6b in contrast with d for $c \geq 10^{-2}$).

We also show that the SP effects on conjugate margin width depend on the underlying rheology at the start of extension: thermal blanketing more strongly affects weaker and thicker crust. This is reflected in wider ductile domains for WQ models when compared with equivalent GR and AN models where sediment thickness is the same (Figure 6b). In the stronger models, there is little variation on margin width (Figures 6 and 7). We can not yet rule out that even models with sea can reproduce larger effects of SP on margin width and conjugate symmetry for rheologies weaker than the ones explored in this study.

4.2. Rifting and Surface Processes in Nature

In nature, margins portray a large variability in their architecture, including width of the conjugate margins, fault population characteristics, abruptness of crustal necking, and so forth. It is widely accepted that this variability is the result of differences in the initial lithospheric thermal structure, rheology of the extending lithosphere, initial crustal thickness, distribution of crustal weaknesses, extension velocities, and magma supply (e.g., Brune et al., 2014; Buck, 1991; Huismans & Beaumont, 2003, 2007, 2014; Hopper et al., 2003; Ros et al., 2017; Svartman Dias et al., 2015; Sharples et al., 2015). In this study we have shown for the first time that variation in erosion and sedimentation rates, as well as in the depositional environment (e.g., sub-aeral vs submarine environments), are key factors in determining margin morphology and rift evolution. This implies that factors such as climate, weathering, and fluvial network evolution may also play a role in architectural styles and rift development. In order to study a particular rift system and reproducing the final margin structure through modeling one should constrain all these parameters. Reproducing the structure of any particular passive margin observed in nature, or identifying the main factor/s responsible of its morphology, will be addressed in future studies. Here, we restrict our discussion to the most essential analogies between models and nature. These comparisons allow us to explain basement features that have yet to be well understood as the potential consequence of interaction between surface processes and extensional tectonics.

One of these features is the large offset faults observed in models with high surface process efficiencies during the early phases of rifting. Potential analogies to this can be observed in natural examples of continental rifts. For instance, the Lake Baikal rift system accounts in some sections for up to 9 km of syn-rift continental lacustrine sediments with limiting faults that have 8–12 km offset and little offsets at intrabasin faults (Hus et al., 2012; Hutchinson et al., 1992). Likewise, in the western branch of the Eastern African rift system, large-offset (~7 km) planar faults separate uplifted flanks from basins containing large lacustrine sediment piles (e.g., up to 6 km in lake Tanganyika; Ebinger, 1989; Morley, 1988). Our modeling results imply that the large fault offsets in these examples can be explained as a result of strain localization due to efficient erosion/sedimentation loading/unloading during the initial phases of rifting.

Thick syn-rift sediments associated with large offset faults are also observed in the proximal sectors of the Great Australian Bight (GAB) margin. Structurally, the GAB is characterized by localization of the crustal thinning around families of large offset border faults (e.g., the Wallaroo fault system), that separate the shelf basement high from a seaward very attenuated continental crust (Ball et al., 2013; Direen et al., 2012; Stagg et al., 1990; Talwani et al., 1979; Totterdell et al., 2000). These fault systems are active during the initial phases of rifting in the Late Jurassic (Totterdell et al., 2000). Large amount of syntectonic sediments are deposited at the hanging walls of the border faults (~4 km), over the crustal necking, and high erosion is observed at the foot-wall (Ball et al., 2013; Direen et al., 2007; Stagg et al., 1990; Totterdell et al., 2000; Totterdell et al., 2003). Furthermore, these sediments were deposited under fluvial and lacustrine environments, at least in the proximal domains of the margin during the early rifting (Totterdell et al., 2000). This could explain why sediments were efficiently transported into the half-grabens developed over the border fault hanging walls, enhancing plastic strain localization and producing efficient crustal thinning as observed in our models with no sea (see Figures S24b, S26b, and S27i–S27j and movies 40AN2nS and 40WQ2nS).

Faulting is scarcely imaged in the basement of the Ceduna basin, seaward from the border faults (i.e., more distal sectors). Here, the large subsidence observed during the Early Cretaceous has been interpreted as the result of a more distal ductile extension phase that could also explain the large beta factors (β >4) at the Ceduna basement with no associated basement faulting (Ball et al., 2013; Totterdell et al., 2000). We suggest that this phase of ductile extension is analogous to the development of pure shear ductile domains in the models under the effects of thermal blanketing associated with the thick overlying supersequences of Bronze Whaler and Blue Whale (Figure 6d), deposited under submarine conditions (Totterdell et al., 2000). The conjugate margin of Wilkes Land (WL) also showcases abrupt thinning of the crust along a faulting zone near the shelf edge, and oceanward an attenuated continental crust with evidence of ductile deformation (i.e., anomalously high subsidence), together with thick syn-rift sediments (Colwell et al., 2006). Furthermore, this pair of conjugate margins is symmetric in terms of width. From the results of the models here presented, we infer that the symmetry and structure observed at the GAB-WL margins could be partly controlled by large syn-rift sedimentation over the proximal and intermediate distal margin sectors, possible due to a delayed marine incursion (i.e., AN and WQ for $c \geq 10^{-2}$ in Figure 6 and Figures S24b, S26b, and S27i–S27j and movies 40AN2nS and 40WQ2nS).

Anomalous post-Valanginian regional subsidence is also observed in the Northern Carnarvon basin in the absence of synchronous faulting at the upper crust (Driscoll & Karner, 1998). This margin also showcases thick syn-rift sequences. This anomalous subsidence has been interpreted as the result of lower crustal thinning through a low angle detachment (Driscoll et al., 1995; Karner et al., 2003). This interpretation could be equivalent to the low-angle low viscosity shear zone that forms in our tests with high subaerial SP efficiencies and sea (e.g., narrow margin in Figures 4j–4l).

The Angola margin highlights a distal domain covered by sag basin sediments where evidences of faulting are not present ("Continental Slope Domain" in Aslanian et al., 2009, and "Exhumation and Outer Domains" of Figure 6 in Péron-Pinvidic et al., 2015). Péron-Pinvidic et al. (2015) interpret these regions as areas of possible exhumation of the mantle without ruling out the presence of overlying transitional crust. Another interpretation is that here the basement consists of unstructured lower crust that has deformed ductilely (Aslanian et al., 2009; Karner et al., 2003). One of the arguments against this last interpretation is that, as crust extends and thins, it cools leading to a complete embrittlement of the crust (Pérez-Gussinyé et al., 2001, 2003). However, our models show that this can only occur for low sedimentation rates, such in the West Iberia margin, because otherwise the thermal insulation associated to sedimentation (i.e., hotter basement) would inhibit cooling and keep the LC ductile (e.g., Figures 5b–5d). Our models with AN 40-km (Figures 4h and 4l), show a distal ductile zone with exhumed LC. These distal parts could be analogous to those of the Angola margin which presents a thick sag basin sequence, with planar reflectors off-lapping toward the top-basement (Karner et al., 2003; Péron-Pinvidic et al., 2015; Rowan, 2018), implying that there was enough syntectonic deposition to favor a final phase of ductile crustal extension associated with thermal blanketing. Note that, in our models, sediment thickness required for the formation of ductile domains is smaller for weaker than for stronger LCs (Figure 6), implying that lower crustal strength is also an important factor for the formation of the distal ductile domains.

Margin width changes are observed along axis in the Gulf of California (Lizarralde et al., 2007). These changes have been interpreted as the result of either along-axis changes in sedimentation and/or man-

tle fertility (Bialas & Buck, 2009; Lizarralde et al., 2007). Narrow margins develop in the northern sector (Delfín-Tiburón and Guaymas sector) under thick sediments supplied from the Colorado River, while wide margins develop in the south central sector (Alarcon sector) under thin sediment packages (González-Fernández et al., 2005; Lizarralde et al., 2007; Martín-Barajas et al., 2013). Our results support the hypothesis that SP can potentially explain the axial variation in margin architecture in the Gulf of California, where high sedimentation rates would favor the localization of the deformation and fast crustal thinning in the proximal areas (Figure 6d and Figures S22, S24, and S26). Based on the thick magmatic crust observed in the Guaymas sector, Lizarralde et al. (2007) proposed that thermal blanketing associated with high sedimentation rates combined with fertile mantle result in large volumes of melting that lead to abrupt crustal breakup. On the contrary, Bialas and Buck (2009) suggested that sedimentation would push the isotherms down in the area of deformation and thermal blanketing would occur only for areas of abandoned deformation. In theory, this would lead to colder crustal-sediment column, that together with sediment loading would favor narrow rifting. However, the narrow rifting phase in Bialas and Buck (2009) is active for a prolonged period of time without crustal breakup generating a very attenuated crust (i.e., Figure 10 in Bialas & Buck, 2009), and localization of the deformation seems to occur exclusively within the mantle. To our knowledge, narrow rifting mechanisms are incompatible with the production of large attenuated crustal domains. The modeled margins shown in this work also showcase wide attenuated ductile domains seaward from the point of abrupt crustal necking under large sediment loads (Figure 6d and Figures S22, S24, and S26). However, these domains are the byproduct of a final phase of pure-shear or rift-migration ductile extension, and not of narrow rifting. It is likely that the higher resolution of our models (from 1 km to 100 m in very thin layers vs 4 km), together with our efforts to differentiate viscous from plastic deformation, allow for the observation of these ductile domains and the effects of thermal blanketing. In agreement with Lizarralde et al. (2007), our results show that high sedimentation rates heat the crust and mantle, potentially enhancing melt generation that could intrude thinned ductile crust and accelerate breakup.

Clearly, natural examples show striking analogies to some model outcomes. This is not to say that the structure and symmetry/asymmetry of passive margins is exclusively conditioned by the efficiency of surface processes or contrasting subaerial/submarine deposition. We agree that tectonic inheritance, rift dynamics, thermal state, and lithospheric strength can all play major roles in the geometric configuration of passive margins, as shown by previous works. However, in this work we have shown that realistic distinct surface process efficiencies can potentially lead to variations in margin architecture of similar magnitude to the ones inferred for the other tectonic factors.

5. Conclusions

In this work we have tested the influence of surface processes on rifting structures and the final architecture of rifted margins. For this purpose, we developed a state-of-the-art numerical model that solves for deformation, temperature, and pressure for a layered visco-elasto-plastic lithosphere, and coupled it to a landscape evolution model that accounts for sediment transport under subaerial and submarine environments. With this model we conducted a broad parametric study in which we tested the interactions of different subaerial surface processes efficiencies with different lower crustal rheologies and initial crustal thicknesses.

In agreement with previous works, we find that surface processes promote the localization of the plastic deformation due to the reduction in topographic and flexural forces that oppose fault displacement. Consequently, high erosion and sedimentation rates favor longer-lived faults, larger faulted blocks, and abrupt crustal necking, analogous to observations at the proximal margins from the Great Australian Bight and its conjugate Wilkes Land, the Gulf of California, and strongly sedimented continental rifts such as Baikal and Tanganyika. Conversely, we find that intermediate to high sedimentation rates over hot extending crustal sectors (i.e., late rifting and distal margins) exert an effect of thermal blanketing that favors viscous distributed deformation at the basement and leads to the formation of unstructured attenuated crustal domains, such as the basements of the Ceduna basin in the Great Australian Bight, and the Carnarvorn basins in western Australia, and possibly the distal domains of Angola margin. These ductile domains typically develop in more distal margin sectors and during the last rifting phases, most likely under submarine conditions. Here, we note that these unstructured attenuated crustal domains could be easily misinterpreted in seismic sections as part of the continent-ocean transition.

Our experiments show that the timing of the marine incursion may play an important role in the final conjugate geometry for models with weaker lithosphere (i.e., 40-km-thick crust models). These models tend to develop asymmetric conjugate margins by migration of deformation during late rifting stages resulting in wide and narrow conjugated margins. Early marine incursion implies damping of sediment transport into the distal extending areas and, therefore, low syn-rift sedimentation during rift migration. However, due to the asymmetry of deformation, sediments from the narrow margin would be more efficiently supplied to the extending area. If subaerial sediment transport efficiency is rapid enough, sediment supply from the future narrow margin would lead to larger and longer-lived basinward dipping faults located in this area, so that sequential faulting starts later in the margin's evolution. Some of these faults would be transferred to the future wide margin through rift migration, resulting in a final wide margin which contains sequential in time oceanward dipping faults in the basement and landward dipping faults in the overlying sediments that were induced by sediment loading of the narrow margin. Thermal blanketing in the last rifting stages could further result in ductile deformation of the entire crust, generating distal domains of unstructured basement that juxtapose sediments on top of lower crustal rocks. In models with sea, we observe much less change in conjugate margin asymmetry because the reduction in domains that behave partly brittlely is counteracted by an increase in width of domains that behave fully ductilely.

Conversely, equivalent models with no sea highlight increasing symmetry and decreasing margin width with increasing surface process efficiency because more efficient sediment transport into extending areas aids strain localization at the center of the model. This is in agreement with observations from Great Australian Bight, where a continental environment dominated the early and intermediate rifting stages. We suggest that the timing of the marine incursion into a rift may play an important role on the evolution and final architecture of margins. These results also suggest that factors such as climate, the geographic locus of rifting (i.e., in the middle of a super-continent vs a back-arc) and the precursor fluvial network could all play important roles on shaping the structure and symmetry/asymmetry of passive margins.

References

Allen, J., & Beaumont, C. (2016). Continental margin syn-rift salt tectonics at intermediate width margins. *Basin Research*, *28*(5), 598–633. https://doi.org/10.1111/bre.12123

Andrés-Martínez, M., Morgan, J. P., Pérez-Gussinyé, M., & Rüpke, L. (2015). A new free-surface stabilization algorithm for geodynamical modelling: Theory and numerical tests. *Physics of the Earth and Planetary Interiors*, *246*, 41–51. https://doi.org/10.1016/j.pepi.2015.07.003

Armitage, J. J., Allen, P. A., Burgess, P. M., Hampson, G. J., Whittaker, A. C., Duller, R. A., & Michael, N. A. (2015). Sediment transport model for the Eocene Escanilla sediment-routing system: Implications for the uniqueness of sequence stratigraphic architectures. *Journal of Sedimentary Research*, *85*(12), 1510–1524. https://doi.org/10.2110/jsr.2015.97

Armitage, J., Duller, R., & Schmalholz, S. (2014). The influence of long-wavelength tilting and climatic change on sediment accumulation. *Lithosphere*, *6*(5), 303–318. https://doi.org/10.1130/L343.1

Armitage, J. J., Jaupart, C., Fourel, L., & Allen, P. A. (2013). The instability of continental passive margins and its effect on continental topography and heat flow. *Journal of Geophysical Research: Solid Earth*, *118*, 1817–1836. https://doi.org/10.1002/jgrb.50097

Aslanian, D., Moulin, M., Olivet, J., Unternehr, P., Matias, L., Bache, F., et al. (2009). Brazilian and African passive margins of the central segment of the South Atlantic Ocean: Kinematic constraints. *Tectonophysics*, *468*(1), 98–112. https://doi.org/10.1016/j.tecto.2008.12.016

Ball, P., Eagles, G., Ebinger, C., McClay, K., & Totterdell, J. (2013). The spatial and temporal evolution of strain during the separation of Australia and Antarctica. *Geochemistry, Geophysics, Geosystems*, *14*, 2771–2799. https://doi.org/10.1002/ggge.20160

Bialas, R. W., & Buck, R. W. (2009). How sediment promotes narrow rifting: Application to the Gulf of California. *Tectonics*, *28*, TC4014. https://doi.org/10.1029/2008TC002394

Bos, B., & Spiers, C. J. (2002). Frictional-viscous flow of phyllosilicate-bearing fault rock: Microphysical model and implications for crustal strength profiles. *Journal of Geophysical Research*, *107*(B2), 2028. https://doi.org/10.1029/2001JB000301

Brune, S., Heine, C., Pérez-Gussinyé, M., & Sobolev, S. V. (2014). Rift migration explains continental margin asymmetry and crustal hyper-extension. *Nature Communications*, *5*, 4014. https://doi.org/10.1038/ncomms5014

Brune, S., Popov, A. A., & Sobolev, S. V. (2012). Modeling suggests that oblique extension facilitates rifting and continental break-up. *Journal of Geophysical Research*, *117*, B08402. https://doi.org/10.1029/2011JB008860

Buck, W. R. (1991). Modes of continental lithospheric extension. *Journal of Geophysical Research*, *96*(B12), 20,161–20,178. https://doi.org/10.1029/91JB01485

Buck, W. R. (1993). Effect of lithospheric thickness on the formation of high- and low- angle normal faults. *Geology*, *21*(10), 933–936. https://doi.org/10.1130/0091-7613(1993)021<0933:EOLTOT>2.3.CO;2

Buck, W. R., & Lavier, L. L. (2001). A tale of two kinds of normal fault: The importance of strain weakening in fault development. *Geological Society, London, Special Publications*, *187*, 289–303. https://doi.org/10.1144/GSL.SP.2001.187.01.14

Buck, W. R., & Poliakov, A. N. (1998). Abyssal hills formed by stretching oceanic lithosphere. *Nature*, *392*, 272–275. https://doi.org/10.1038/32636

Buiter, S. J. H., Huismans, R. S., & Beaumont, C. (2008). Dissipation analysis as a guide to mode selection during crustal extension and implications for the styles of sedimentary basins. *Journal of Geophysical Research*, *113*, B06406. https://doi.org/10.1029/2007JB005272

Burov, E., & Cloetingh, S. (1997). Erosion and rift dynamics: New thermomechanical aspects of post-rift evolution of extensional basins. *Earth Planetary Science Letters*, *150*(1-2), 7–26. https://doi.org/10.1016/S0012-821X(97)00069-1

Burov, E., & Poliakov, A. (2001). Erosion and rheology controls on synrift and postrift evolution: Verifying old and new ideas using a fully coupled numerical model. *Journal of Geophysical Research*, *106*(B8), 16,461–16,481. https://doi.org/10.1029/2001JB000433

Christensen, N. I., & Mooney, W. D. (1995). Seismic velocity structure and composition of the continental crust: A global view. *Journal of Geophysical Research*, *100*(B6), 9761–9788. https://doi.org/10.1029/95JB00259

Clift, P. D., Brune, S., & Quinteros, J. (2015). Climate changes control offshore crustal structure at South China Sea continental margin. *Earth and Planetary Science Letters*, *420*, 66–72. https://doi.org/10.1016/j.epsl.2015.03.032

Colwell, J. B., Stagg, H. M., Direen, N. G., Bernardel, G., & Borissova, I. (2006). The structure of the continental margin off Wilkes Land and Terre Adélie coast, east Antarctica, *Antarctica* (pp. 327–340). Berlin, Heidelberg: Springer.

Contrucci, I., Matias, L., Moulin, M., Géli, L., Klingelhofer, F., Nouzé, H., et al. (2004). Deep structure of the West African continental margin (Congo, Zaïre, Angola), between 5°S and 8°S, from reflection/refraction seismics and gravity data. *Geophysical Journal International*, *158*(2), 529–553. https://doi.org/10.1111/j.1365-246X.2004.02303.x

Culling, W. (1960). Analytical theory of erosion. *The Journal of Geology*, *68*(3), 336–344.

Dabrowski, M., Krotkiewski, M., & Schmid, D. W. (2008). MILAMIN: MATLAB-based finite element method solver for large problems. *Geochemistry, Geophysics, Geosystems*, *9*, Q04030. https://doi.org/10.1029/2007GC001719

de Souza Neto, E. A., Perić, D., & Owen, D. R. J. (2008). *Computational methods for plasticity: Theory and applications* (Vol. 6, pp. 137–190). John Wiley. https://doi.org/10.1002/9780470694626.ch6

Dean, S. M., Minshull, T. A., Whitmarsh, R. B., & Louden, K. E. (2000). Deep structure of the ocean-continent transition in the southern Iberia Abyssal Plain from seismic refraction profiles: The IAM-9 transect at 40°20′N. *Journal of Geophysical Research*, *105*(B3), 5859–5885.

Dietrich, W. E., Bellugi, D. G., Sklar, L. S., Stock, J. D., Heimsath, A. M., & Roering, J. J. (2003). Geomorphic transport laws for predicting landscape form and dynamics, *Prediction in geomorphology* (Vol. 135, pp. 103–132). Washington, DC: American Geophysical Union. https://doi.org/10.1029/135GM09

Direen, N. G., Borissova, I., Stagg, H. M. J., Colwell, J. B., & Symonds, P. A. (2007). Nature of the continent-ocean transition zone along the southern Australian continental margin: A comparison of the Naturaliste Plateau, SW Australia, and the central Great Australian Bight sectors. *Geological Society, London, Special Publications*, *282*(1), 239–263. https://doi.org/10.1144/SP282.12

Direen, N. G., Stagg, H. M. J., Symonds, P. A., & Norton, I. O. (2012). Variations in rift symmetry: Cautionary examples from the Southern Rift System (Australia-Antarctica). *Geological Society, London, Special Publications*, *369*(1), 453–475. https://doi.org/10.1144/SP369.4

Driscoll, N. W., Hogg, J. R., Christie-Blick, N., & Karner, G. D. (1995). Extensional tectonics in the Jeanne d'Arc Basin, offshore Newfoundland: Implications for the timing of break-up between Grand Banks and Iberia. *Geological Society, London, Special Publications*, *90*(1), 1–28. https://doi.org/10.1144/GSL.SP.1995.090.01.01

Driscoll, N., & Karner, G. (1998). Lower crustal extension across the northern Carnarvon Basin, Australia: Evidence for an eastward dipping detachment. *Journal of Geophysical Research*, *103*(B3), 4975–4991. https://doi.org/10.1029/97JB03295

Ebinger, C. (1989). Tectonic development of the western branch of the East African rift system. *Geological Society of America Bulletin*, *101*(7), 885–903.

França, G. S., & Assumpção, M. (2004). Crustal structure of the Ribeira fold belt, SE Brazil, derived from receiver functions. *Journal of South American Earth Sciences*, *16*(8), 743–758. https://doi.org/10.1016/j.jsames.2003.12.002

Gleason, G. C., & Tullis, J. (1995). A flow law for dislocation creep of quartz aggregates determined with the molten salt cell. *Tectonophysics*, *247*(1), 1–23. https://doi.org/10.1016/0040-1951(95)00011-B

González-Fernández, A., Dañobeitia, J. J., Delgado-Argote, L. A., Michaud, F., Córdoba, D., & Bartolomé, R. (2005). Mode of extension and rifting history of upper Tiburón and upper Delfín basins, northern Gulf of California. *Journal of Geophysical Research*, *110*, B01313. https://doi.org/10.1029/2003JB002941

Graf, W. H. (1984). *Hydraulics of sediment transport*. Littleton, CO: Water Resources Publication.

Handy, M. R., & Stünitz, H. (2002). Strain localization by fracturing and reaction weakening—A mechanism for initiating exhumation of subcontinental mantle beneath rifted margins. *Geological Society, London, Special Publications*, *200*(1), 387–407. https://doi.org/10.1144/GSL.SP.2001.200.01.22

Hansen, L. N., Zimmerman, M. E., & Kohlstedt, D. L. (2012). Laboratory measurements of the viscous anisotropy of olivine aggregates. *Nature*, *492*, 415–418. https://doi.org/10.1038/nature11671

Hirth, G., & Kohlstedt, D. (2003). Rheology of the upper mantle and the mantle wedge: A view from the experimentalists. In G. Hirth & D. Kohlstedt (Eds.), *Inside the subduction factory* (pp. 83–105). Washington, DC: American Geophysical Union. https://doi.org/10.1029/138GM06

Hopper, J. R., Dahl-Jensen, T., Holbrook, W. S., Larsen, H. C., Lizarralde, D., Korenaga, J., et al. (2003). Structure of the SE Greenland margin from seismic reflection and refraction data: Implications for nascent spreading center subsidence and asymmetric crustal accretion during North Atlantic opening. *Journal of Geophysical Research*, *108*(B5), 2269. https://doi.org/10.1029/2002JB001996

Hopper, J., Funck, T., & Tucholke, B. (2007). Structure of the Flemish Cap margin, Newfoundland: Insights into mantle and crustal processes during continental breakup. *Geological Society, London, Special Publications*, *282*(1), 47–61. https://doi.org/10.1144/SP282.3

Howard, A. D. (1994). A detachment-limited model of drainage basin evolution. *Water Resources Research*, *30*(7), 2261–2285. https://doi.org/10.1029/94WR00757

Huffman, G., Adler, R., Bolvin, D., & Gu, G. (2009). Improving the global precipitation record: GPCP version 2.1. *Geophysical Research Letters*, *36*, L17808. https://doi.org/10.1029/2009GL040000

Huismans, R. S., & Beaumont, C. (2003). Symmetric and asymmetric lithospheric extension: Relative effects of frictional-plastic and viscous strain softening. *Journal of Geophysical Research*, *108*(B10), 2496. https://doi.org/10.1029/2002JB002026

Huismans, R. S., & Beaumont, C. (2007). Roles of lithospheric strain softening and heterogeneity in determining the geometry of rifts and continental margins. *Geological Society, London, Special Publications*, *282*(1), 111–138. https://doi.org/10.1144/SP282.6

Huismans, R., & Beaumont, C. (2011). Depth-dependent extension, two-stage breakup and cratonic underplating at rifted margins. *Nature*, *473*, 74–78. https://doi.org/10.1038/nature09988

Huismans, R. S., & Beaumont, C. (2014). Rifted continental margins: The case for depth-dependent extension. *Earth and Planetary Science Letters*, *407*, 148–162. https://doi.org/10.1016/j.epsl.2014.09.032

Hus, R., Poort, J., Charlet, F., Naudts, L., Khlystov, O., Klerkx, J., & De Batist, M. (2012). *Regional geology and tectonics: Phanerozoic rift systems and sedimentary basins*, Lake Baikal (pp. 258–273). B.V: Elsevier. https://doi.org/10.1016/B978-0-444-56356-9.00010-9

Hutchinson, D., Golmshtok, A., Zonenshain, L., Moore, T., Scholz, C., & Klitgord, K. (1992). Depositional and tectonic framework of the rift basins of Lake Baikal from multichannel seismic data. *Geology*, *20*(7), 589–592. https://doi.org/10.1130/0091-7613(1992)020<0589:DATFOT>2.3.CO;2

Karato, S. I., & Wu, P. (1993). Rheology of the upper mantle: A synthesis. *Science*, *260*(5109), 771–778.

Karner, G. D., Driscoll, N. W., & Barker, D. H. N. (2003). Syn-rift regional subsidence across the West African continental margin: The role of lower plate ductile extension, *Petroleum geology of Africa: New themes and developing technologies* (Vol. 207, pp. 105–129). Geological Society of London. https://doi.org/10.1144/GSL.SP.2003.207.6

Kaufman, P., Grotzinger, J. P., & McCormick, D. S. (1991). Depth-dependent diffusion algorithm for simulation of sedimentation in shallow marine depositional systems. *Bulletin - Kansas Geological Survey*, *233*, 489–508.

Kaus, B. J. P. (2010). Factors that control the angle of shear bands in geodynamic numerical models of brittle deformation. *Tectonophysics*, *484*(1), 36–47. https://doi.org/10.1016/j.tecto.2009.08.042

Kaus, B. J. P., Mühlhaus, H., & May, D. A. (2010). A stabilization algorithm for geodynamic numerical simulations with a free surface. *Physics of the Earth and Planetary Interiors*, *181*(1), 12–20. https://doi.org/10.1016/j.pepi.2010.04.007

Kirkby, M. J. (1971). Hillslope process-response models based on the continuity equation. *Special Publication Institute of British Geographers*, *3*(1), 15–30.

Kirkby, M. J., & Carson, M. A. (1972). *Hillslope form and process*. Cambridge: Cambridge University Press.

Lavier, L. L., & Manatschal, G. (2006). A mechanism to thin the continental lithosphere at magma-poor margins. *Nature*, *440*, 324–328. https://doi.org/10.1038/nature04608

Lizarralde, D., Axen, G., Brown, H., Fletcher, J., González-Fernández, A., Harding, A., et al. (2007). Variation in styles of rifting in the Gulf of California. *Nature*, *448*, 466–469. https://doi.org/10.1038/nature06035

Marr, J., Swenson, J., Paola, C., & Voller, V. (2000). A two-diffusion model of fluvial stratigraphy in closed depositional basins. *Basin Research*, *12*(3-4), 381–398. https://doi.org/10.1111/j.1365-2117.2000.00134.x

Martín-Barajas, A., González-Escobar, M., Fletcher, J., Pacheco, M., Oskin, M., & Dorsey, R. (2013). Thick deltaic sedimentation and detachment faulting delay the onset of continental rupture in the Northern Gulf of California: Analysis of seismic reflection profiles. *Tectonics*, *32*, 1294–1311. https://doi.org/10.1002/tect.20063

McClay, K. R. (1977). Pressure solution and Coble creep in rocks and minerals: A review. *Journal of the Geological Society*, *134*(1), 57–70. https://doi.org/10.1144/gsjgs.134.1.0057

Moresi, L., Dufour, F., & Mühlhaus, H. B. (2003). A Lagrangian integration point finite element method for large deformation modeling of viscoelastic geomaterials. *Journal of Computational Physics*, *184*(2), 476–497. https://doi.org/10.1016/S0021-9991(02)00031-1

Morgan, J. P. (1997). The generation of a compositional lithosphere by mid-ocean ridge melting and its effect on subsequent off-axis hotspot upwelling and melting. *Earth and Planetary Science Letters*, *146*(1), 213–232. https://doi.org/10.1016/S0012-821X(96)00207-5

Morgan, J. P., Morgan, J. W., & Price, E. (1995). Hotspot melting generates both hotspot volcanism and a hotspot swell? *Journal of Geophysical Research*, *100*(B5), 8045–8062. https://doi.org/10.1029/94JB02887

Morley, C. K. (1988). Variable extension in Lake Tanganyika. *Tectonics*, *7*(4), 785–801. https://doi.org/10.1029/TC007i004p00785

Morley, C. K., & Westaway, R. (2006). Subsidence in the super-deep Pattani and Malay basins of Southeast Asia: A coupled model incorporating lower-crustal flow in response to post-rift sediment loading. *Basin Research*, *18*(1), 51–84. https://doi.org/10.1111/j.1365-2117.2006.00285.x

Nielsen, T. K., & Hopper, J. R. (2004). From rift to drift: Mantle melting during continental breakup. *Geochemistry, Geophysics, Geosystems*, *5*, Q07003. https://doi.org/10.1029/2003GC000662

Olive, J., Behn, M., & Malatesta, L. (2014). Modes of extensional faulting controlled by surface processes. *Geophysical Research Letters*, *41*, 6725–6733. https://doi.org/10.1002/2014GL061507

Paola, C., Heller, P. L., & Angevine, C. L. (1992). The large-scale dynamics of grain-size variation in alluvial basins, 1: Theory. *Basin Research*, *4*(2), 73–90.

Parmentier, E. M, & Morgan, J. P. (1990). Spreading rate dependence of three-dimensional structure in oceanic spreading centres. *Nature*, *348*, 325–328. https://doi.org/10.1038/348325a0

Pérez-Gussinyé, M. (2013). A tectonic model for hyperextension at magma-poor rifted margins: An example from the West Iberia–Newfoundland conjugate margins. *Geological Society, London, Special Publications*, *369*(1), 403–427. https://doi.org/10.1144/SP369.19

Pérez-Gussinyé, M., Ranero, C. R., Reston, T. J., & Sawyer, D. (2003). Mechanisms of extension at nonvolcanic margins: Evidence from the Galicia interior basin, west of Iberia. *Journal of Geophysical Research*, *108*(B5), 2245. https://doi.org/10.1029/2001JB000901

Pérez-Gussinyé, M., Reston, T. J., & Phipps Morgan, J. (2001). Serpentinization and magmatism during extension at non-volcanic margins: The effect of initial lithospheric structure. *Geological Society, London, Special Publications*, *187*(1), 551–576. https://doi.org/10.1144/GSL.SP.2001.187.01.27

Péron-Pinvidic, G., Manatschal, G., Masini, E., Sutra, E., Flament, J., Haupert, I., & Unternehr, P. (2015). Unravelling the along-strike variability of the Angola-Gabon rifted margin: A mapping approach. *Geological Society, London, Special Publications*, *438*(1), SP438.1. https://doi.org/10.1144/SP438.1

Petit, C., Fournier, M., & Gunnell, Y. (2007). Tectonic and climatic controls on rift escarpments: Erosion and flexural rebound of the Dhofar passive margin (Gulf of Aden, Oman). *Journal of Geophysical Research*, *112*, B03406. https://doi.org/10.1029/2006JB004554

Précigout, J., & Gueydan, F. (2009). Mantle weakening and strain localization: Implications for the long-term strength of the continental lithosphere. *Geology*, *37*(2), 147–150. https://doi.org/10.1130/G25239A.1

Ranero, C. R., & Pérez-Gussinyé, M. (2010). Sequential faulting explains the asymmetry and extension discrepancy of conjugate margins. *Nature*, *468*(7321), 294–299. https://doi.org/10.1038/nature09520

Redfield, T. F., & Osmundsen, P. T. (2013). The long-term topographic response of a continent adjacent to a hyperextended margin: A case study from Scandinavia. *Geological Society of America Bulletin*, *125*(1-2), 184–200. https://doi.org/10.1130/B30691.1

Ros, E., Pérez-Gussinyé, M., Araújo, M., Romeiro, M., Andrés-Martínez, M., & Morgan, J. (2017). Lower crustal strength controls on melting and serpentinization at magma-poor margins: Potential implications for the South Atlantic. *Geochem Geophys Geosystems*, *18*(12), 4538–4557. https://doi.org/10.1002/2017GC007212

Rowan, M. (2018). The South Atlantic and Gulf of Mexico salt basins: Crustal thinning, subsidence and accommodation for salt and presalt strata. *Geological Society, London, Special Publications*, *476*, SP476.6. https://doi.org/10.1144/SP476.6

Rutter, E., & Elliott, D. (1976). The kinetics of rock deformation by pressure solution. *Philosophical Transactions of the Royal Society of London A: Mathematical, Physical and Engineering Sciences*, *283*(1312), 203–219.

Rybacki, E., & Dresen, G. (2000). Dislocation and diffusion creep of synthetic anorthite aggregates. *Journal of Geophysical Research*, *105*(B11), 26,017–26,036. https://doi.org/10.1029/2000JB900223

Schutt, D., & Lesher, C. (2006). Effects of melt depletion on the density and seismic velocity of garnet and spinel lherzolite. *Journal of Geophysical Research*, *111*, B05401. https://doi.org/10.1029/2003JB002950

Sharples, W., Moresi, L.-N., Jadamec, M., & Revote, J. (2015). Styles of rifting and fault spacing in numerical models of crustal extension. *Journal of Geophysical Research: Solid Earth*, *120*, 4379–4404. https://doi.org/10.1002/2014JB011813

Shewchuk, J. R. (2002). Delaunay refinement algorithms for triangular mesh generation. *Computational Geometry*, *22*(1–3), 21–74. https://doi.org/10.1016/S0925-7721(01)00047-5

Simpson, G., & Schlunegger, F. (2003). Topographic evolution and morphology of surfaces evolving in response to coupled fluvial and hillslope sediment transport. *Journal of Geophysical Research*, *108*(B6), 2300. https://doi.org/10.1029/2002JB002162

Smith, T. R., & Bretherton, F. P. (1972). Stability and the conservation of mass in drainage basin evolution. *Water Resources Research*, *8*(6), 1506–1529. https://doi.org/10.1029/WR008i006p01506

Stagg, H., Willcox, J., Needham, D., O'Brien, G., Cockshell, C., Hill, A., et al. (1990). Basins of the Great Australian Bight region-geology and petroleum potential: Continental margins. *Bureau of Mineral Resources, Geology and Geophysics and Department of Mines and Energy, South Australia*. Australian Government Publishing Service.

Svartman Dias, A., Lavier, L., & Hayman, N. (2015). Conjugate rifted margins width and asymmetry: The interplay between lithospheric strength and thermomechanical processes. *Journal of Geophysical Research: Solid Earth*, *120*, 8672–8700. https://doi.org/10.1002/2015JB012074

Talwani, M., Mutter, J., Houtz, R., & Konig, M. (1979). The crustal structure and evolution of the area underlying the magnetic quiet zone on the margin south of Australia: Rifted margins. In *Geological and geophysical investigations of continental margins* (pp. 151–175). AAPG Special Volumes.

Theissen, S., & Rüpke, L. (2010). Feedbacks of sedimentation on crustal heat flow: New insights from the Vøring Basin, Norwegian Sea. *Basin Research*, *22*(6), 976–990. https://doi.org/10.1111/j.1365-2117.2009.00437.x

Totterdell, J., Blevin, J., Struckmeyer, H., Bradshaw, B., Colwell, J., & Kennard, J. (2000). A new sequence framework for the Great Australian Bight: Starting with a clean slate. *APPEA Journal-Australian Petroleum Production and Exploration Association*, *40*(1), 95–120. https://doi.org/10.1071/AJ99007

Totterdell, J., Bradshaw, B., & Willcox, J. (2003). Structural and tectonic setting of the Great Australian Bight. In G. W. O'Brien, E. Paraschivoiu, & J. E. Hibburt (Eds.), *Petroleum geology of South Australia* (Vol. 5, pp. 1–57). South Australia: Primary Ind. and Resour.

Turcotte, D., & Schubert, G. (2002). *Geodynamics*. Cambridge: Cambridge University Press.

Weissel, J. K., & Karner, G. D. (1989). Flexural uplift of rift flanks due to mechanical unloading of the lithosphere during extension. *Journal of Geophysical Research*, *94*(B10), 13,919–13,950. https://doi.org/10.1029/JB094iB10p13919

Wilks, K., & Carter, N. (1990). Rheology of some continental lower crustal rocks. *Tectonophysics*, *182*(1-2), 57–77.

Zwaan, F., Schreurs, G., & Adam, J. (2018). Effects of sedimentation on rift segment evolution and rift interaction in orthogonal and oblique extensional settings: Insights from analogue models analysed with 4D X-ray computed tomography and digital volume correlation techniques. *Global and Planetary Change*, *171*, 110–133. https://doi.org/10.1016/j.gloplacha.2017.11.002